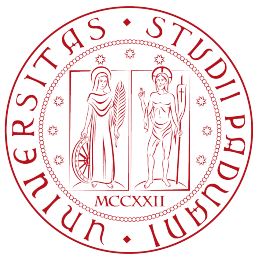

Università degli Studi di Padova

Dipartimento di Ingegneria Industriale

Corso di Laurea Magistrale in
Ingegneria Elettrica

PM vs PM-less motor topologies for electric vehicles: a comparative analysis

Relatore:
Prof. Nicola Bianchi

Laureando:
Fabio Filippini
2024016

Correlatore:
Mr. Luca Cinti

Anno Accademico 2022/2023

Sommario

Con l'aumentare della domanda di veicoli elettrici, l'industria automobilistica si sta concentrando nello sviluppo di powertrain più efficienti e sostenibili. In questa tesi, si confrontano le prestazioni di diverse tipologie di motori elettrici che richiedono quantità ridotte o nulle di magneti permanenti. La seguente analisi include studi elettromagnetici e termici, volti a identificare i limiti di funzionamento di ciascuna macchina. In particolare, si considera, come termine di paragone, un motore a magneti permanenti in NdFeB (IPM), confrontandolo con altri motori come un Wound Rotor (WR), un Hybrid Excited Permanent Magnet (HEPM), un motore a riluttanza (REL) e uno a riluttanza assistita da magneti in ferrite (PMaREL). Oltre al confronto tra i motori, si discutono anche le tendenze recenti nel campo della trazione, inclusa la spinta verso tecnologie più ecologiche e sostenibili. Si esplora la crescente tendenza tra i produttori di motori a ridurre la loro dipendenza dai magneti permanenti e si analizzano i vantaggi e gli svantaggi dell'utilizzo di progetti alternativi. Le conclusioni forniscono preziosi spunti sulle caratteristiche prestazionali delle diverse tipologie di motori elettrici presentate e possono guidare progettisti e produttori di motori nella loro ricerca di sviluppare powertrain per veicoli elettrici più efficienti e sostenibili, mantenendosi al passo con le ultime tendenze del settore.

Abstract

The automotive industry is focusing on developing more efficient and sustainable powertrains due to the increasing demand for electric vehicles. In this thesis, we compare the performance of different electric motor topologies that require fewer or no permanent magnets. Our analysis includes both electromagnetic and thermal studies aimed at identifying the limits of operation of each machine. Specifically, we compare the Interior Permanent Magnet (IPM) motor, which utilizes NdFeB magnets, with various permanent magnet-free motor designs such as the Wound Rotor (WR) motor and Hybrid Excited Permanent Magnet (HEPM) motor. In addition to the motor comparison, we also discuss recent trends in the field of traction, including the push for more environmentally friendly and sustainable technologies. We explore the growing trend among motor manufacturers to reduce their reliance on permanent magnets and discuss the benefits and drawbacks of using alternative motor designs. Our findings provide valuable insights into the performance characteristics of permanent magnet-free electric motor topologies and can guide motor designers and manufacturers in their quest to develop more efficient and sustainable EV powertrains, while keeping up with the latest trends in the industry.

List of acronyms

AC: Alternating Current

BM: Bonded Magnets

CPSR: Constant Power Speed Range

DC: Direct Current

EMF: Electromotive Force

EV: Electric Vehicle

FEM: Finite Element Method

FW: Flux Weakening

HEPM: Hybrid Excitation Permanent Magnet

HEV: Hybrid Electric Vehicle

IM: Induction Motor

IPM: Interior Permanent Magnet

MTPA: Maximum Torque Per Ampere

MTPV: Maximum Torque Per Voltage

PM: Permanent Magnet

PMaREL: Permanent Magnet assisted Reluctance

PMSM: Permanent Magnet Synchronous Motor

pf: Power Factor

PWM: Pulse Width Modulation

REL: Reluctance

WR: Wound Rotor

List of Figures

List of Tables

Contents

Chapter 1

Introduction

The electrification of vehicle powertrains has emerged as a practical solution for improving energy efficiency and reducing greenhouse gas emissions in the automotive industry. The popularity of electric vehicles (EVs) has increased significantly since the successful launch of the Toyota Prius in 1997. Today, major car manufacturers such as Honda, Nissan, Ford, Mercedes, BMW, and others offer EV models.

The competition brought by EVs has driven innovation in the auto industry, leading to significant improvements in gasoline-powered cars as well. However, Tesla has emerged as a leader in terms of innovation and competition in the EV market. The proliferation of EVs has been driven by several factors, including advances in electric power, battery components, and charging infrastructure, market competition, and government incentives.

To meet the demanding requirements of EVs, electric machines used in their powertrains must have several critical features. They must be highly efficient, have large rated and starting torque, a wide speed range, large overload capacity, large power at cruising speeds, constant power speed, high specific power and power density, high reliability, and good fault tolerance. These requirements apply to all types of electric machines used in EVs, but the specific design and control measures depend on the machine's topology and operating principle.

Ultimately, the machine that meets all of these requirements must also be cost-effective. The topology and operating principle of the machine will dictate the specific design and control measures required to meet these requirements. In conclusion, the electrification of vehicle powertrains has revolutionized the automotive industry, and the continued innovation and advancement of electric machines will undoubtedly continue to shape the industry's future.

1.1 Electric motors in the automotive industry

The following table displays the specification parameters of recent automobiles, which have been collected from various sources. Although placing this data side by side can provide some insight, it is challenging to make meaningful comparisons between these values without taking into account the drive system architecture and/or hybridization strategy of the vehicle. Additionally, there are differences in the machines themselves, such as the use of one versus two machines, which further complicates the comparison process. It is important to mention certain observed patterns, including the tendency to move away from Induction Machines (IM) and towards Permanent Magnet (PM) machines in the majority of traction applications.

Regarding the IM machine, the rotor copper losses are as significant as the stator copper losses and are challenging to cool. The IM motor exhibits lower efficiency and torque density, and a higher weight compared to a PM with the same current density.

Furthermore, in Table 1.1, it can be observed that both the Tesla Roadster and the Model S

utilize a 4-pole IM motor. Since the frequency is proportional to the pole number for a given speed, and both the inverter loss and motor iron losses increase with frequency, the practical choices for the pole number are usually limited to two or four poles (for IM motors). To maintain the same flux density in the stator and rotor yokes, the yoke thickness in a two-pole machine would need to be twice that of a four-pole machine. Therefore, in a two-pole machine, for the same outer diameter, the rotor must have a smaller diameter than a four-pole motor, resulting in a higher torque production for the four-pole motor. Thus, the yoke of a 4-pole IM motor will certainly be thicker than that of a permanent magnet motor with a higher number of poles, consequently leading to a higher weight and a lower torque density. PM motors have several drawbacks, including high cost, limited availability of rare-earth magnets, and potential demagnetization under certain operating conditions.

Table 1.1: Traction machines in the market

Model	Year	Motor type	Peak power [kW]	Peak torque [Nm]	Max speed [rpm]	poles
Tesla Roadster	2008	IM	215	370	14000	4
Tesla Model S	2013	IM	225	430	14800	4
Tesla Model 3	2017	PM	192	410	18000	6
Toyota Prius	2004	PM	50	400	6000	8
Toyota Prius	2010	PM	60	207	13500	8
Toyota Prius	2017	PM	53	163	17000	8
Chevrolet Volt	2016	PM	111	370	12000	12
Chevrolet Bolt	2017	PM	150	360	8810	8
Lexus RX	2008	PM	110	300	10230	8
Renault Zoe	2013	WR	100	245	11300	4
BMW i3	2016	PM	125	250	11400	12
BMW iX3	2021	WR	-	-	-	6

1.2 Recent trends in electric machines in electric vehicles

1.2.1 Machines with rare-earth magnets

As mentioned above, the electrical vehicle trend is to use synchronous motors. The motors can have PM mounted on the rotor or not according to the power density. There is no doubt about the capability of motors that utilize a significant amount of heavy rare-earth content to meet the essential performance requirements of traction motors. Most of these motors have been equipped with rare-earth magnets, specifically in the form of Interior Permanent Magnet (IPM) machines. The IPM machines have gained significant popularity in traction drive systems due to their ability to generate both permanent magnet torque and reluctance torque, as well as achieve a wide Constant Power Speed Range (CPSR) operation.

IPM machines can be designed to generate reluctance torque in the range of 40-50% or even higher, which is an incredibly appealing feature for traction applications. Consequently, IPM machines have become the preferred choice for such applications, and this preference is expected to persist. One would have assumed that with the availability of high reluctance torque, the use of magnets in these machines would have stabilized over time, particularly considering that the cost of magnets constitutes around 20-30% of the total motor cost. It would be reasonable to expect manufacturers to be interested in reducing motor costs by reducing magnet usage. However, contrary to expectations, the use of magnets has not decreased and may have actually increased over the years.

1.2.2 Machines without rare-earth magnets

There is a significant trend in the design of electric vehicle machines towards exploring alternatives that do not rely on rare-earth magnets. By eliminating the need for rare-earth magnets, not only can motor cost reduction be achieved, but also the dependence on this critical material can be eliminated. While induction machines have been considered as potential alternatives, the increasing demands for high specific power and power density requirements are rendering them less viable options.

Two important machine topologies that eliminate magnets on the rotor are the synchronous reluctance (REL) machine and the wound rotor machine (WR). REL machines have a simple construction, with the rotor composed of thin steel laminations. On the other hand, WR machines offer appealing features such as robustness, high efficiency, low torque ripple, and simplicity (resulting in low cost) of control.

It seems that with extensive research and development, REL and WR machines have the potential to offer high-performance traction machines without relying on rare-earth content.

1.2.3 Hairpin winding

An increasing trend in electric machinery is to employ hairpin windings, which consist of preformed rectangular bars that are inserted into slots and joined at one end. Hairpin windings are manufactured and assembled differently from traditional stranded windings. This can result in lower production costs and better consistency because the position and placement of each conductor are precisely controlled and known. Additionally, the end windings are usually more compact in hairpin winded machines. Hairpin windings offer a higher slot fill factor over stranded windings. This particular winding has a reduced phase resistance as a result of an enlarged conductor cross-section, so the DC winding losses are reduced in comparison to traditional windings. Although DC losses are reduced in the hairpin winding, the AC winding losses are significantly higher. Consequently, the total winding losses in the hairpin winding are greater. The AC losses are closely linked to the radial turn height, so it is preferable to minimize the conductor height to reduce AC loss. Unfortunately, this is limited by the manufacturing aspect ratio of the conductor. Using hairpin technology enables a more compact design and a better utilization of the available space envelope, however due to the higher AC losses efficiency will be dropped at higher speed ranges. From a manufacturing and practical standpoint, the elevated AC copper losses are attributed to the limited number of conductors that can fit within a slot, typically ranging from 8 to 12. As a result, the eddy current phenomenon plays a significant role and cannot be disregarded in high-frequency motor applications. Thus, it is imperative to accurately calculate the AC losses during the design phase to properly assess the motor's thermal performance (see Appendix C).

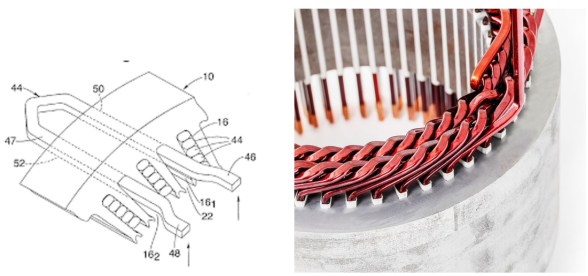

Figure 1.1: Hairpin winding example [3]

1.2.4 Machine and power electronics integration

This is another growing trend that will persist. As the need for more comfortable vehicles increases, powertrain devices must become smaller, and consequently, innovative integration techniques become more crucial. The concept of physically combining the electric machine and power electronic drive into a single enclosure (package) offers not only compactness and reduced size but also easy installation, fewer components, shorter cable runs and busbars. All of these factors can lead to desirable technical advantages, such as reduced electromagnetic interference, decreased voltage overshoots on motor drive terminals, and significant cost savings.

For example the BMW i3 has the inverter mounted above the motor (Figure 1.2).

Figure 1.2: BMW i3 motor and inverter assembly [9]

1.3 Rare-Earth Magnet Price Volatility

Around 95% of the world's neodymium is exported from China, which raises two concerns. Firstly, the extraction process of this material has a significant environmental impact. Secondly, relying heavily on a single country and region for such a large portion of the world's supply creates a risk of price uncertainty. In 2011, there was a drastic increase in the price of neodymium by over 20 times, which caused significant financial strain for both large and small companies. Consequently, there was a push to find alternative machine topologies to replace synchronous machines that use sintered NdFeB magnets. The next chapter introduces the major alternative synchronous machine configurations that are the subject of this thesis. These include PM synchronous machines that use either much smaller amounts of NdFeB magnets as well as synchronous reluctance machines and electrically excited synchronous machines that require no magnets at all. These motors have unique features that can make them suitable for specific applications, and they are expected to play an increasingly important role in the future of electric motor technology.

1.4 Thesis Outline

This thesis focuses on the design and analysis of permanent magnet motors and alternative motor designs for EV traction. The primary objective is to evaluate the performance characteristics of these motors and identify the strengths and weaknesses of each design.

To compare different machines, it is useful to talk about torque density instead of power density because the former is a function of the magnetic force generated in the air gap, while the latter depends on the speed, which can be easily influenced by factors such as nominal frequency and voltage. For example, doubling the nominal frequency or the supply voltage results in a doubling of speed, and likewise, power density also doubles.

The comparison is made considering equal:

- external dimensions
- materials
- DC joule losses in the stator windings
- winding type: hairpin
- number of conductors in slot
- cooling: liquid

As a benchmark, the well-known permanent magnet motor of the BMW i3 will be used, and its inverter will also be employed for all the machines (the specifications are listed in Table 1.2). The inverter utilizes an Infineon power module rated at 650 V_{DC} and 800 A continuous current, with a peak of 1600 A [12].

The decision has been made to utilize hairpin windings for all the machines, resulting in rectangular-shaped stator slots to maximize the slot fill factor (approximately 65% for all the machines). The copper losses are calculated considering a temperature of 120°C. Additionally, liquid cooling will be employed.

For each machine, a concise theory overview will be presented to emphasize the parameters with the most significant influence on its performance, followed by electromagnetic and thermal analyses.

The objective was to attain a torque of approximately 200 Nm for the IPM motor, leading to the determination of the corresponding current density and DC stator joule losses. Subsequently, the current densities for the other machines were selected to align with the DC stator joule losses of the IPM motor.

Table 1.2: Inverter characteristics and motor performance requirements

Parameter	Symbol	Value	Unit
DC bus voltage inverter	V_{DC}	650	V
Continuous phase current	I	800	A
Peak phase current	I_{peak}	1600	A
Base speed	n_b	4000	rpm
Max speed	n_{max}	16000	rpm

1.4.1 Motors analyzed in this study

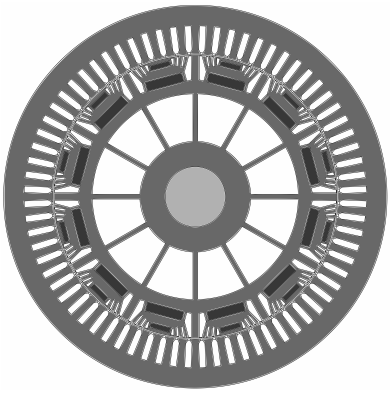

IPM: This is the motor of the iconic BMW i3, which I will use as a benchmark. The rotor's geometry is derived from a scan of the original, while I redesigned the stator to accommodate hairpin windings, which are characterized by rectangular slots.

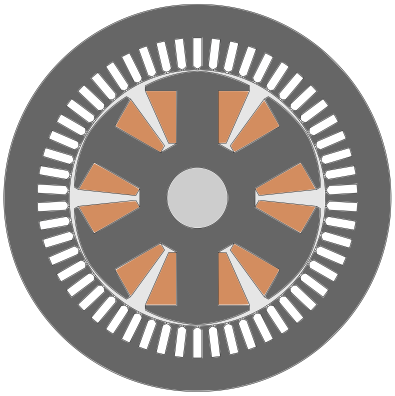

WR: This aims to represent the motor of the BMW iX3, even though specific information about this machine is not publicly available.

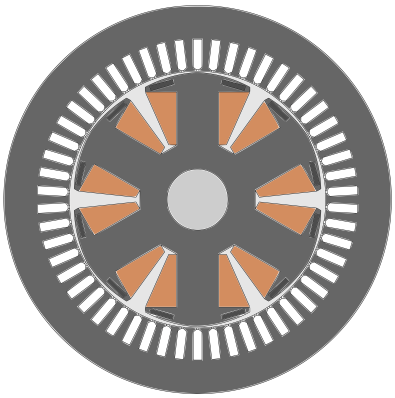

HEPM: To explore the possibility of using hybrid rotor structures, I attempted to place two small NdFeB magnets on each pole, aiming to increase the torque density of the machine.

REL: Synchronous reluctance motors are a promising technology which has features that are aligned with the previously mentioned industrial needs, that is, high efficiency and low cost. However, they present some disadvantages that may not make them ideal for electric traction, and these aspects will be analyzed in this study.

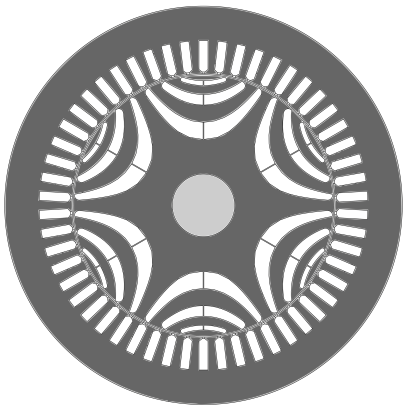

PMaREL: One way to increase the torque density of a REL machine is by incorporating bonded magnets made of ferrite into the flux barriers. These magnets are less performance-intensive compared to NdFeB magnets, but they are also less expensive.

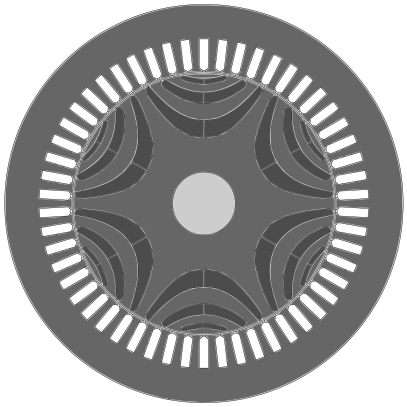

Chapter 2

PM synchronous machines

The majority of traction motors utilize rare earth permanent magnets (PMs) such as NdFeB, with the addition of Dysprosium to enhance temperature stability. These PMs are embedded in the iron of the rotor, creating what is known as an IPM (Interior Permanent Magnet) rotor. This motor demonstrates a high torque density and a relatively wide constant-power speed range. Nonetheless, employing rare earth PMs results in a significant expense for the motor. Permanent magnet (PM) motors have become the preferred choice in various types of electric vehicles due to their numerous advantages, including high efficiency compared to other machine types, high torque density, and superior reliability. However, the maximum torque output of a permanent magnet machine is restricted by the machine and converter's maximum supported current, while the maximum speed is limited by the maximum voltage supplied by the power electronics. To achieve the desired current, the voltage can be regulated. However, as the machine reaches its base speed, the voltage hits its limit. To increase speed further, a field weakening technique is employed, which involves adjusting the angle between the current and back EMF to introduce a negative current on the *d*-axis. This causes demagnetization in the armature reaction field within the gap, weakening the magnetic field generated by the magnets, and expanding the constant power region. It should be noted that introducing a negative current on the *d*-axis decreases the nominal torque.

The operation of PM machines is based on the permanent magnets torque, to which is added the contribution of the reluctance torque, due to the anisotropy of the rotor. Two magnetic paths can be identified in the rotor: the first is the one with minimum reluctance, or maximum inductance, and the second is with maximum reluctance. Using the *dq* coordinates, the d axis is the one aligned with the magnet flux linkage phasor Λ_m that corresponds to the low-inductance axis since the permanent magnets have an incremental permeability value very close to that of air, resulting in a low value of *d*-axis inductance L_{d}, in contrast, magnetic flux oriented along the *q*-axis does not have to cross any of the magnet cavities, resulting in a higher value of inductance for L_{q}.

2.1 Motor model and operating condition

The steady-state voltage equations of a synchronous motor in the *dq* rotating reference frame are:

$$\begin{aligned} V_d &= R_s I_d - \omega_m^e L_{\mathrm{q}} I_q \\ V_q &= R_s I_{q+} \omega_m^e (\Lambda_m + L_{\mathrm{d}} I_d) \end{aligned} \tag{2.1}$$

where V_d, V_q, I_d, I_q are the stator voltages and currents respectively, L_{d}, L_{q} are the motor inductances, Rs is the stator resistance, Λ_m is the PM flux linkage and $\omega_m^e = p\omega_m$ are the electrome-

chanical speed, pole pairs and mechanical speed. In the following analytical analysis magnetic saturation, iron losses and PM demagnetisation effects are neglected. The steady-state electromechanical torque can be computed as below, where two terms can be recognized: the PM and the reluctance torque.

$$T = \frac{3}{2} p[\Lambda_m I_q + (L_\mathrm{d} - L_\mathrm{q}) I_d I_q] \tag{2.2}$$

An analysis of the motor operation can be carried out by drawing the (2.1) and (2.2) in the $I_d - I_q$ plane. In that plane, (2.2) defines, for each torque, a hyperbola whose asymptotes are the axis $I_q = 0$ and the vertical line centered in $I_d = -\Lambda_m/(L_\mathrm{d} - L_\mathrm{q})$. The latter lies in the positive I_d semiplane, since all IPM motors have $L_\mathrm{q} > L_\mathrm{d}$. By considering the inverter capabilities, the current limit defines a circle in the $I_d - I_q$ plane, centered in the plane origin, and given by:

$$I_d^2 + I_q^2 \leq I_n^2 \tag{2.3}$$

and the voltage limit defines an ellipse, centered in $(-\Lambda_m/L_\mathrm{d}, 0)$, where the ratio $-\Lambda_m/L_\mathrm{d}$ is equal to the magnitude of the steady-state three-phase short-circuit current. The ellipticity is equal to the saliency ratio $\xi = L_\mathrm{q}/L_\mathrm{d}$ and the ellipse equation is expressed by 2.4.

$$V_N^2 = \omega_m^{e\ 2}[(\Lambda_m + L_\mathrm{d} I_d)^2 + (L_\mathrm{q} I_q)^2] \tag{2.4}$$

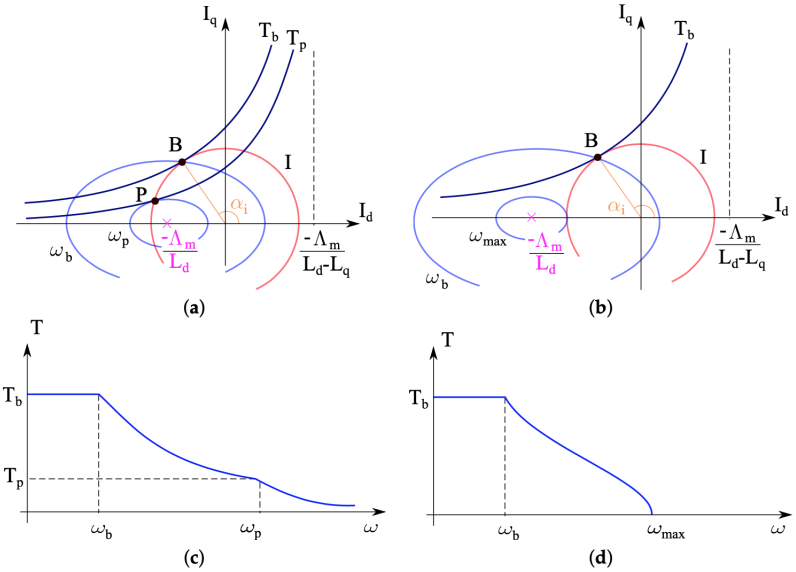

Figure 2.1: Circle diagrams and torque versus speed characteristic when electric motors have $\Lambda_m > L_\mathrm{d} I_N$ or $\Lambda_m < L_\mathrm{d} I_N$. (a) Circle diagram with $\Lambda_m < L_\mathrm{d} I_N$. (b) Circle diagram with $\Lambda_m > L_\mathrm{d} I_N$. (c) Torque vs speed $\Lambda_m < L_\mathrm{d} I_N$.(d) Torque vs speed with $\Lambda_m > L_\mathrm{d} I_N$. [6]

Fig. 2.1 shows two circle diagrams with two different short-circuit current levels. The rated current limit circle, two voltage limit ellipses (drawn for rated voltage and two different motor speeds), and some constant torque hyperbolas are shown. Operating points which lie outside either the current limit circle or the voltage limit ellipse, do not comply with drive voltage and current limitations. Rated torque T_b is the maximum torque which can be obtained by rated current. The base speed ω_b (in electrical rad/s) is the speed at which the drive delivers rated torque with rated voltage. The two quantities, T_b and ω_b, are associated with the hyperbola and the ellipse crossing the point B in Fig. 2.1.

A Synchronous Motor Drive, as described in Fig. 2.2, has three operating regions:

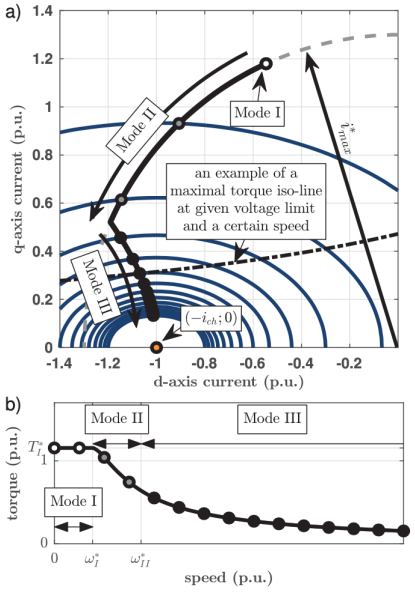

(a) IPM infinite maximum speed drive field weakening operation: a) operation points locus in the *dq*- current space vector plane (the dark blue solid lines are the voltage limitation curves for different speeds), b) corresponding torque vs. speed curve

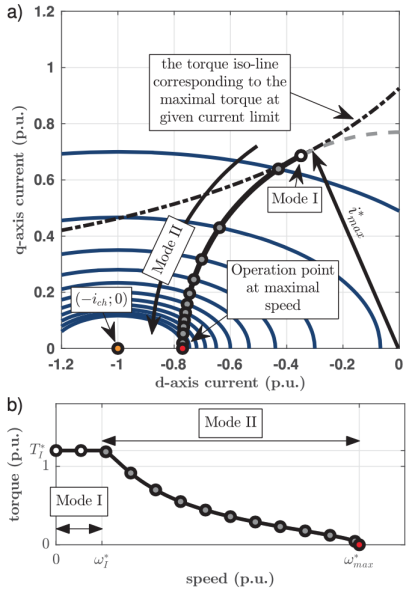

(b) IPM finite maximum speed drive field weakening operation: a) operation points locus in the *dq*- current space vector plane (the dark blue solid lines are the voltage limitation curves for different speeds at constant maximal voltage), b) corresponding torque vs. speed curve

Figure 2.2: Comparison of IPM drive field weakening operations with current trajectories in the *dq* plane [7]

1. *Maximum Torque Per Ampere Region:* (Mode I) for each constant torque loci, there's an optimal operating point which minimizes the Joule losses. In particular MTPA trajectory is obtained as the tangent points between current circles and torque hyperbola, so for any current amplitude, the current angle α_i should be chosen equal to:

$$\alpha_i = \arccos\left(\frac{-\Lambda_m + \sqrt{\Lambda_m^2 + 8(L_\mathrm{d} - L_\mathrm{q})^2 I^2}}{4(L_\mathrm{d} - L_\mathrm{q})I}\right) \tag{2.5}$$

2. *Flux-Weakening: Constant Maximum Available Volt-Ampere Region:* (Mode II) this region starts from the base point B (see also Fig. 2.1) along the current limit circle, towards the point $(-I_N, 0)$, keeping a constant Volt-Ampere rating. If the voltage ellipse center lies outside the current limit circle (see Fig. 2.1 (b) and (d), and Fig. 2.2 (b)), the point $(-I_N, 0)$ can be reached, where the motor exhibits zero torque. This condition corresponds to the higher achievable speed:

$$\omega_{max} = \frac{V_N}{\Lambda_m - L_\mathrm{d} I_N} \tag{2.6}$$

On the contrary, if the center of the voltage ellipse lies within the current limit circle (refer to Fig. 2.1 (a) and (c), and Fig. 2.2 (a)), the movement of the current point along the limit circle reaches point P (see Fig. 2.1 (a) and (c)). In this case, the drive demonstrates its maximum torque-to-voltage ratio, and the corresponding electrical speed ω_p represents the maximum

speed of the FW constant volt-ampere region. Beyond this speed, the control strategy needs to be altered to ensure a feasible working condition.

3. *Flux-Weakening: Decreasing Volt-Ampere Region:* (Mode III) this one exists only for those machines whose ellipse center lies within the current circle (see Fig. 2.1 (a) and (c), and Fig. 2.2 (a)). Above the speed ω_p, torque performances are limited by the voltage limit ellipse. So, it is not possible to proceed moving the current along the current limit circle. The drive current must be decreased in order to respect the voltage limit ellipse, the Maximum Torque per Voltage (MTPV) trajectory takes place. The theoretical maximum speed is infinite.

With a permanent magnet motor, the flux weakening technique is used to exceed the base speed. This technique involves increasing the advance angle of the stator current to saturate the steel in front of the magnets, thereby reducing the flux linkage in the stator windings and the back EMF. In this way, in the total produced torque, the component due to the magnets is reduced, while the reluctance component becomes more important.

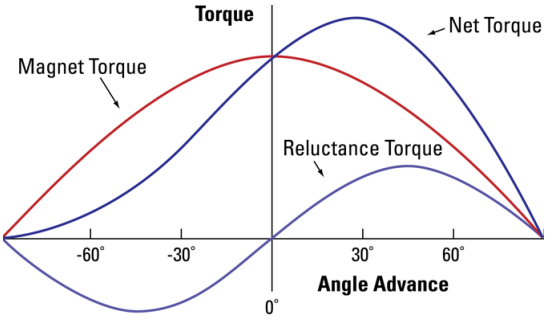

Figure 2.3: PM vs reluctance torque

2.2 BMW i3 IPM machine: analysis

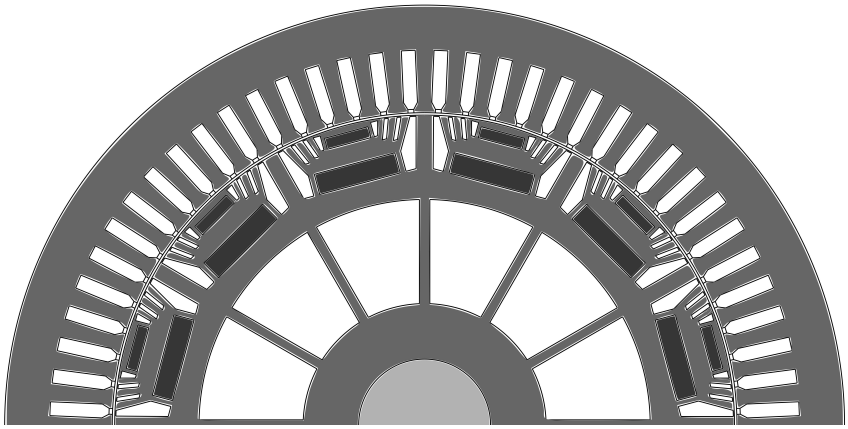

Figure 2.4: IPM motor configuration

Automotive manufacturers usually do not provide detailed information about the design, functionality, and operation of EV/HEV technologies. Even the published details and specifications need to be verified and clarified. For instance, power ratings for motors and inverters are often given as single values, but they do not include information about the power capability throughout the operating range, the duration for which this power can be maintained, the efficiency across the operating region, and other important characteristics. Therefore, I obtained the characteristics of this motor by consulting the report "Oak Ridge National Laboratory, FY 2016 Annual Progress Report for Electric Drive Technologies" [12] [9]. The machine described is one with the highest torque density, also produced by a top-tier manufacturer, exemplifying the capabilities of this technology.

There are two models of this car:

- Pure electric, where the traction motor acts as a generator during braking.
- Electric version with a "range extender" that includes a separate internal combustion engine generator with an active transistor voltage regulator.

Flux carriers and barriers between PM pole produce a significant reluctance torque component thereby reducing the required magnet mass.

The main design parameters are shown in Table 2.1. The rotor and stator core are all made of the same material, M-19 29 Gauge steel. The magnets utilized are sintered neodymium-iron-boron (N35), providing a balance between cost and high magnetic output.

The fact that it has 12 poles and a maximum speed of 11400 rpm indicates that the maximum frequency of the inverter, rounded to 12000 rpm, should be 1200 Hz. This frequency is unusually high for a traction motor. It is important to remember that this is the fundamental frequency of the back EMF, but the carrier frequency of the inverter will be at least 20 times higher, so at least 24 kHz. This is why multilevel inverters are often used, where multiple switches per leg are used, so that each switch operates at a lower frequency than what is seen by the motor.

Table 2.1: i3 IPM geometry parameters

Parameter	Symbol	Value	Unit
Stator slots	Q_s	72	-
Pole number	2p	12	-
Outer diameter	D_e	242	mm
Inner diameter	D_i	180	mm
Stack length	L_{stk}	132	mm
Air gap	g	0.7	mm
Shaft diameter	D_{sh}	38	mm
Back-iron heigth	h_{bi}	13	mm
Slot heigth	h_s	18	mm
Open slot width	w_{so}	1.7	mm
Wed heigth	h_{wed}	2	mm
Tooth width	w_t	3.85	mm
Slot width	w_s	4	mm
Stator fill factor	k_{fill}	0.65	-
Stator slot area	S_{slot}	65.7	mm^2
Stator conductors in slot	n_c	8	-
Parallel stator paths	n_{pp}	4	-
Excitation turns	n_{cs}	2	-
PM1 thickness	t_{m1}	3.3	mm
PM1 length	l_{m1}	12.8	mm
PM2 thickness	t_{m2}	6	mm
PM2 length	l_{m2}	24	mm
PM total volume	V_{PM}	0.000295	m^3

The model's simulation results are displayed in Figure 2.5. It is essential to note that the steel used in the simulation quickly saturates above 1.25 T. The first plot in the figure indicates saturation at the magnet sides when no currents are applied to the windings. This is a crucial aspect of every IPM design, as it produces high reluctance for the leakage flux path around the magnet sides, forcing the magnetic flux out of the rotor through the air gap. Even in the absence of current, the rotor yoke exhibits saturation at a flux return path, indicating high core material utilization. The second plot depicts the state when the windings receive currents that result in the rated torque of the drive. It can be observed that these currents cause significant saturation in the stator yoke and stator teeth.

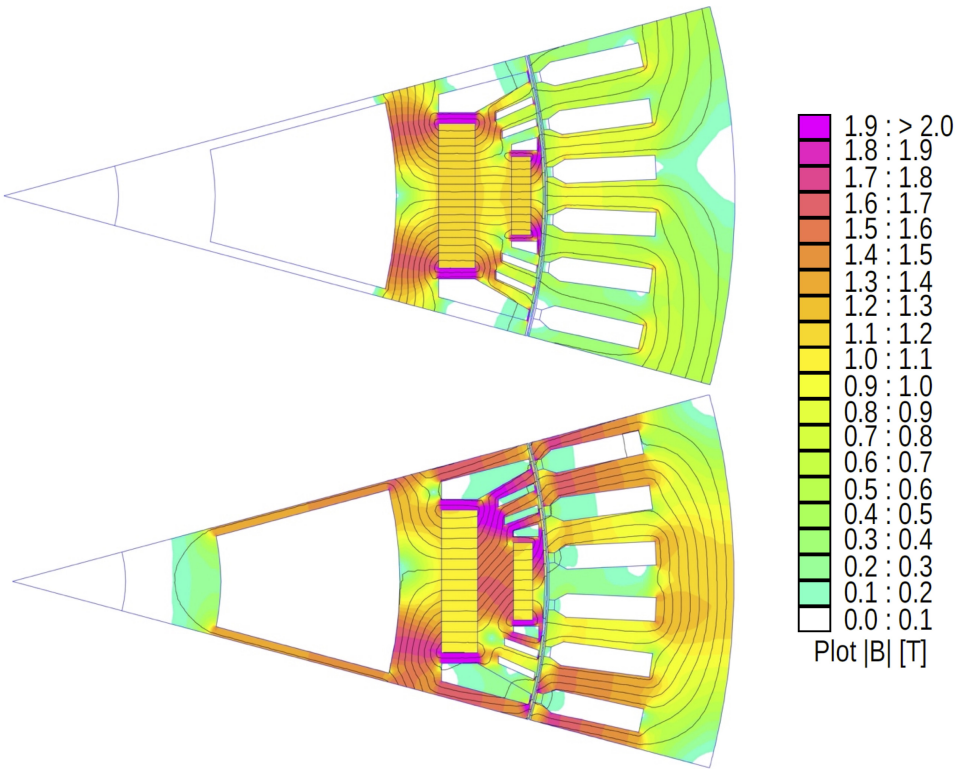

Figure 2.5: Flux density plot at no current state (up) vs peak torque point (down)

The open-circuit air-gap flux density waveform is given in Figure 2.6.

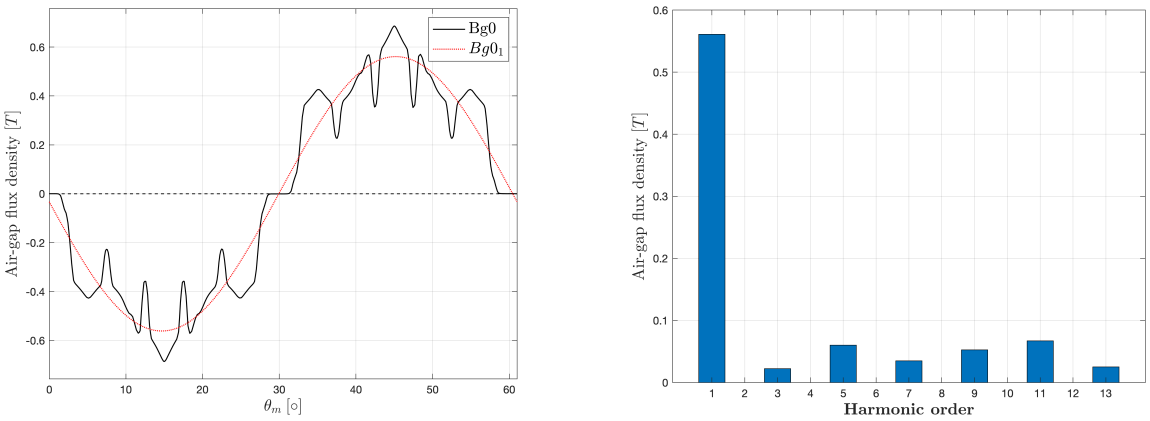

(a) Flux density plot

(b) Harmonic content

Figure 2.6: IPM motor air-gap flux density

An intriguing way to observe a synchronous machine is to represent the torque hyperbolas, current and voltage limits, and track the current vector trajectories on an *idq* plane. In Figure 2.7 we can observe the MTPA trajectory between the no-load point $(0, 0)A$ and the base point, as it intersects the torque hyperbola at 200Nm. From this point, if we want to increase the speed, the current vector follows the flux weakening trajectory along the current limit. Since the characteristic current in this motor is higher than the supply current, there is no MTPV trajectory. Therefore, the

current vector proceeds along the circumference of the current limit until it intersects the voltage ellipse at 16000rpm.

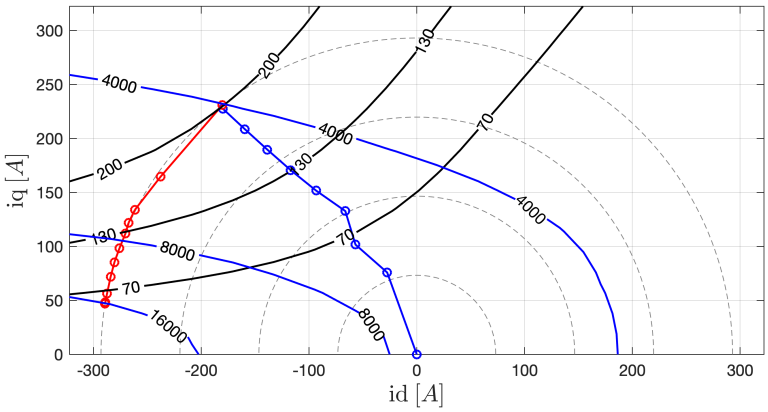

Figure 2.7: MTPA (blue) and FW (red) trajectories

Figure 2.8 illustrates that the surface plot of the q-axis flux linkage exhibits magnetic saturation as the q-axis current component increases. However, the surface plot of the d-axis flux linkage remains relatively linear, with a slight upward curvature observed in the high d-axis current range. This behavior is attributed to the cross-saturation effect, where the d- and q-axis fluxes share a common path in the magnetic circuit. These findings indicate that the modeled machine experiences significant saturation of its iron core within its feasible operating range. Additionally, the figure showcases the incremental inductances, which are the partial derivatives of the dq flux linkages with respect to the current components.

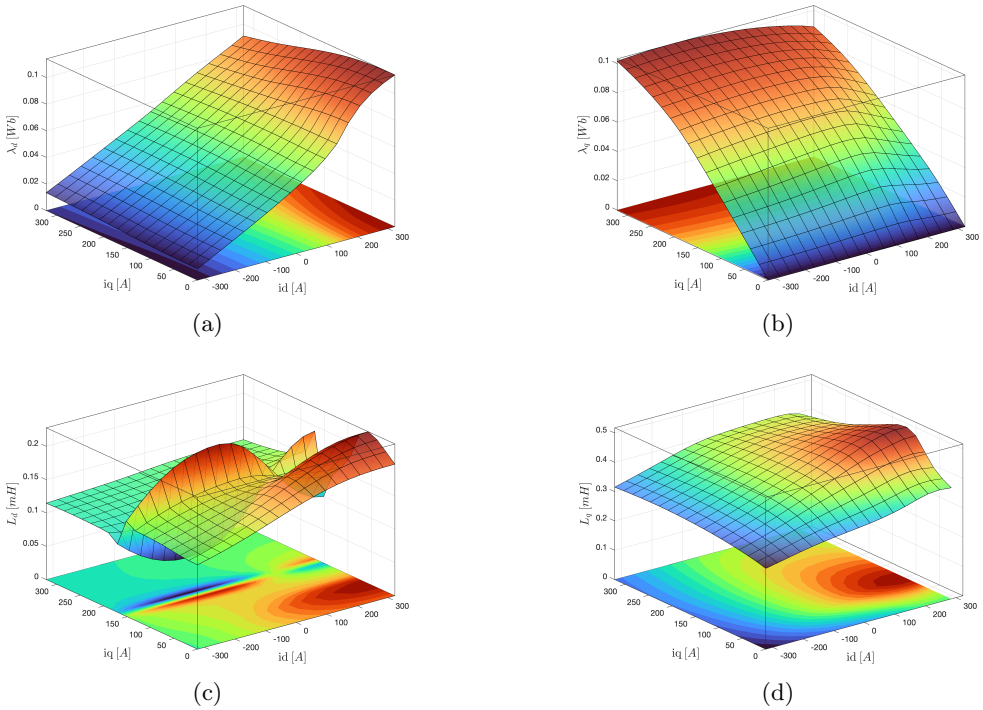

(a) (b) (c) (d)

Figure 2.8: Surface plots: (a) d-axis flux linkage, (b) q-axis flux linkage, (c) d-axis inductance, (d) q-axis inductance

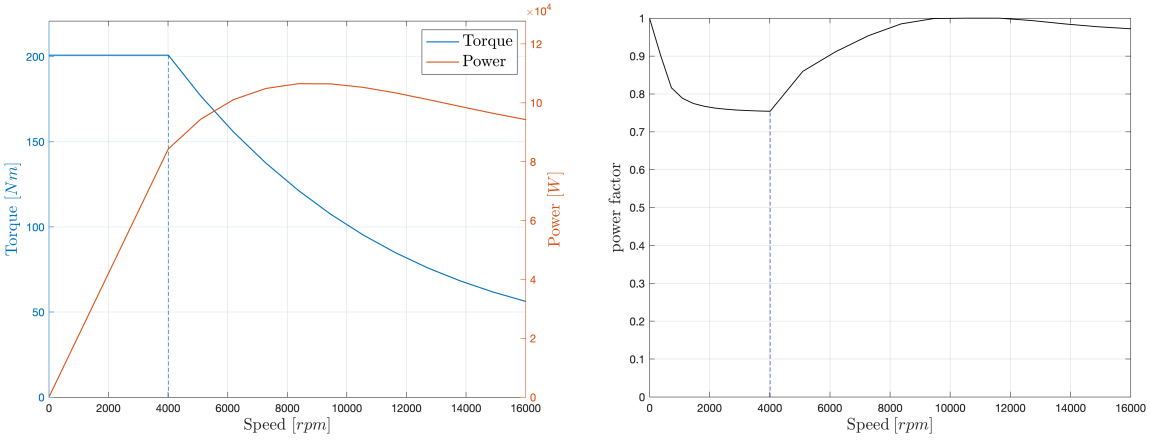

(a) Torque/Power vs Speed (b) Power factor

Figure 2.9: Capability curve and power factor

To assess the mechanical output of a machine, it is customary to plot a torque-speed graph accompanied by a power-speed graph. Figure 2.9a shows that the examined drive demonstrates a single mode of field-weakening operation until the maximum speed of the drive is reached.

Fig. 2.10 shows the torque versus speed characteristic of the motor and the maximum efficiency achievable considering each point on the map. DC voltage supplied is kept constant for values greater than rated speed. The maximum efficiency point is: $\eta = 93.79\%$ To understand how this map was made look at Appendix A

Table 2.2: IPM working point characteristics

Parameter	Symbol	Value	Unit
d-axis inductance	L_d	0.1168	mH
q-axis inductance	L_q	0.3636	mH
saiency	ξ	3.11	/
Base speed	n_b	4000	rpm
Max speed	n_{max}	16000	rpm
Max power	P_{max}	106.46	kW
Phase stator current	Ipeak	293	A
Characteristic current	I_{ch}	431.5	A
DC Joule losses	PJs_{DC}	1682	W
Stator current density	J_s	9.7	A/mm^2

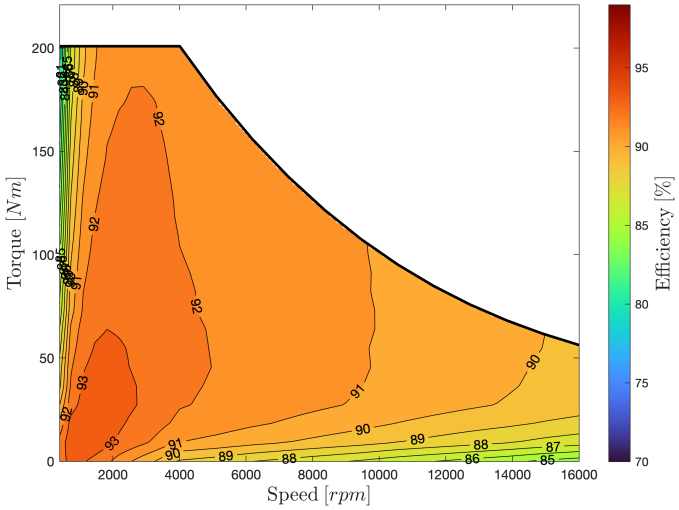

Figure 2.10: Torque versus speed efficiency map

Chapter 3

Wound Rotor synchronous machines

Permanent magnet machines are known for their high power density and are often considered the most efficient electric motors. However, a drawback of these machines is that they lack the ability to turn off the permanent magnets. The magnetic fields of permanent magnets remain constant, which means that when the motor is not actively powered by the energy in the stator winding, it continues to generate energy in the windings, resulting in drag. The proposed drive system stands out for its ability to generate high torque at low speed without overloading the stator windings, and its potential to operate at constant power until reaching unlimited speed. Currently, electric vehicles utilize induction motors or PM synchronous motors in various configurations, along with a suitable power electronic converter. In these types of drives, achieving high torque at low speed requires injecting a substantial amount of current into the stator windings. The maximum torque is generally restricted by the electronic converter's maximum current, which is limited by its high cost per Ampere and poor overload capability in terms of peak current and duration. The common approach to achieve the desired performance at low speed is by oversizing the power electronic converter. However, this approach can result in significant costs, which may render the practical feasibility of drives for heavy electric vehicles powered by a bank of standard lead-acid batteries at low voltage uncertain. The search for the best machine design to achieve constant power operation across a broad speed range has been extensively studied for various Internal Permanent Magnet Synchronous Motor configurations. In these motors, the machine parameters required to achieve constant power operation at high speed do not align with the parameters needed to reach the maximum torque at low speed.

For industrial applications that require constant power operation across a wide range of speeds, the Wound Rotor Synchronous Machine is an alternative solution to IPM machines. WR drives are characterized by their high efficiency, high overload capacity, and excellent performance in the field weakening region. The rotor current of the WR can be independently regulated using a field exciter. In Figure 3.1, the WR drive system is depicted, which incorporates an H-bridge inverter serving as the field exciter. Additionally, the drive system includes a three-phase pulse width-modulation (PWM) inverter. To control the current in the WR, three variables can be utilized: the d-axis stator current, the q-axis stator current, and the field current. The inclusion of the third control variable introduces new possibilities for optimization schemes, such as minimizing losses and enabling distinct safety controls. For example, in the event of a fault during high-speed operation, eliminating the field current can prevent over-voltage in the resulting back-EMF. This unique safety measure safeguards the system from potential damage [10]. It also allows the reduction of iron and excitation losses when operating at partial load. These capabilities combined create a broad operational range with an expanded field weakening area. By using optimal rotor

excitation current control combined with stator field weakening, the WR can achieve above 89% efficiency in almost all operation points above the base point, with a maximum efficiency of over 94%. While the WR's top efficiency is not as high as that of an IPM, its high-efficiency operating area could be larger and better suited for certain uses, and overall, the WR is more efficient than other topologies. The rotor windings can be energized either through conductive connections using slip rings or electromagnetically through a rotary transformer. These machines has high power factor over the whole speed range, which allows a reduced inverter current size and potentially lower drive system cost.

One of the main drawbacks of the WR stems from its primary advantage. The excitation windings in the rotor also result in losses that decrease efficiency and generate heat. The heat generated by the rotor windings is further from the outer surface (presuming an inner rotor), which makes the machine harder to cool.

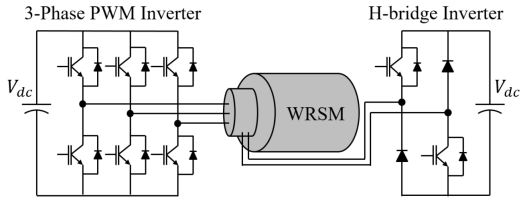

Figure 3.1: Schematic of WR power system [10]

3.1 Motor model and operating condition

Although WR drives present some unique challenges, such as increased rotor losses or more complex mechanical construction compared to other topologies, electrically excited synchronous machines offer distinct advantages that make them suitable for traction applications. The most significant advantage of WR over permanently excited machines is evident in the torque equation.

$$T = \frac{3}{2} p[\Lambda_e I_q + (L_\mathrm{d} - L_\mathrm{q}) I_d I_q] \tag{3.1}$$

The stator flux linkage components are:

$$\begin{aligned} \Lambda_d &= \Lambda_e + L_\mathrm{d} I_d \\ \Lambda_q &= L_\mathrm{q} I_q \end{aligned} \tag{3.2}$$

As shown in 3.2, the rotor flux linkage Λ_d is controllable according to the rotor current and inductance into the d-axis, thus allowing a direct field weakening.

The equations necessary for the study of an WR are the same as those of the PMSM. The wound rotor motor differs because it has $L_\mathrm{d} > L_\mathrm{q}$, therefore the voltage ellipse is rotated with respect to the other case and the saliency is less than one.

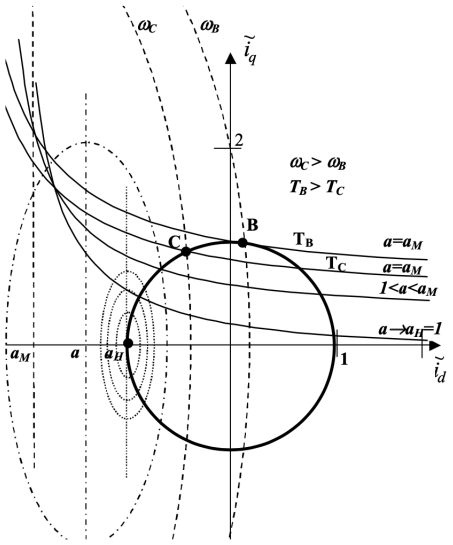

Figure 3.2: Circle diagram with $L_{\mathrm{d}} > L_{\mathrm{q}}$ [15]

The position of the ellipse center varies depending on the excitation current. When the excitation current is increased or decreased, the center of the ellipse moves in the direction of negative id or towards the origin, respectively. When the rotating speed is increased for a given excitation current, the voltage ellipse gradually becomes smaller until it collapses at its origin. In Figure 3.2 , torque hyperbolas, voltage limit ellipses, and current limit circles are displayed using a per unit (p.u.) representation of the current components.

This discussion primarily centers around a control technique aimed at maximizing efficiency across various rotating speeds. When operating at low speeds, the maximum torque per ampere is consistently achieved when the excitation current is at its peak value (100%). However, as the machine operates at high speeds and the voltage reaches its maximum level, efficiency can be enhanced by decreasing the excitation current.

Alternatively, for example, another control technique could be investigated to maximize the power factor across the entire speed range.

3.2 BMW iX3 WR machine: analysis

Limited information is available about the BMW iX3 motor. While the dimensions are similar to those of the BMW i3 motor, there are notable changes in the motor topology. Specifically, the number of poles decreases from 12 to 6, and the number of slots decreases from 72 to 54. Also, it uses hairpin windings.

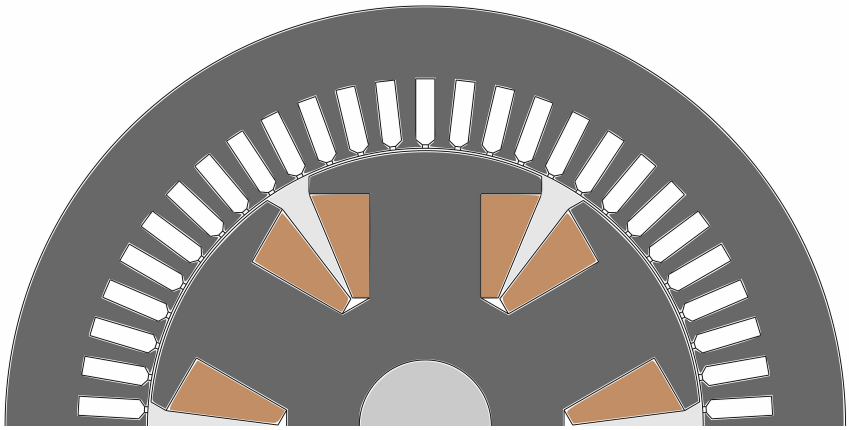

Figure 3.3: WR motor configuration

The decision was made to keep the inverter power ratings, active stack-length, and outer diameter consistent for the proposed machine. The rotor geometry, as it was unknown, was designed to resemble the one described in the paper [11]. Also, the comparison between the machines is conducted based on identical stator joule losses. As mentioned earlier, this machine exhibits a lower torque density, which implies that we anticipate a lower peak torque value.

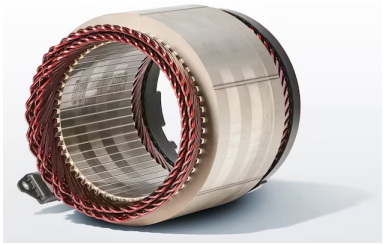

Figure 3.4: BMW iX3 stator [2]

As per BMW, this motor system offers faster switching frequency, and improved heat management. According to BMW, these advancements result in higher RPM, enhanced torque, and increased power. BMW is confident that the utilization of modern materials and sealing technology will enable brushes and commutators to have a satisfactory service life in contemporary electric vehicles [2].

The chosen design parameters are shown in Table 3.1.

Figure 3.5 illustrates the calculated no-load flux linkage of the WR motor in relation to the supplied ampere turns, denoted as $N_e I_e$. When evaluating the performance of the motor, a maximum current density of $J_r = 6.25 A/mm^2$ was utilized.

Table 3.1: Wound-rotor geometry parameters

Parameter	Symbol	Value	Unit
Stator slots	Q_s	54	-
Pole number	2p	6	-
Outer diameter	D_e	242	mm
Inner diameter	D_i	160	mm
Stack length	L_{stk}	132	mm
Minimum air gap	g0	0.7	mm
Shaft diameter	D_{sh}	38	mm
Back-iron heigth	h_{bi}	21	mm
Slot heigth	h_s	20	mm
Open slot width	w_{so}	1.7	mm
Wed heigth	h_{wed}	1.5	mm
Tooth width	w_t	4.97	mm
Slot width	w_s	5.5	mm
Stator fill factor	k_{fill}	0.65	-
Stator slot area	S_{slot}	101.65	mm^2
Stator conductors in slot	n_c	8	-
Parallel stator paths	n_{pp}	3	-
Excitation turns	n_{cs}	2.666	-
Excitation slot area	S_{exc}	337.7	mm^2

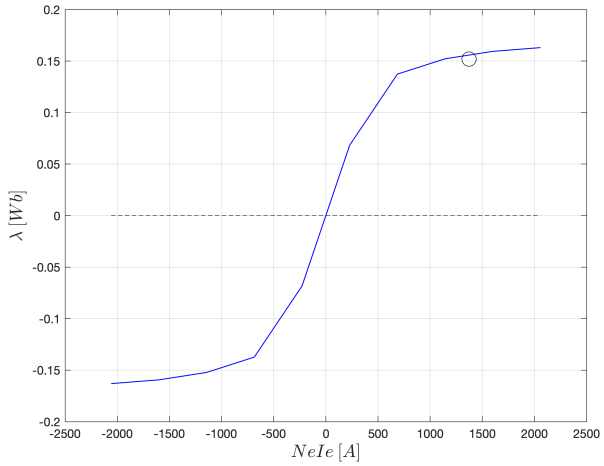

Figure 3.5: No-load flux linkages in relation to the supplied ampere turns

We end up with the following air-gap flux density waveform, which is less sinusoidal than the IPM one:

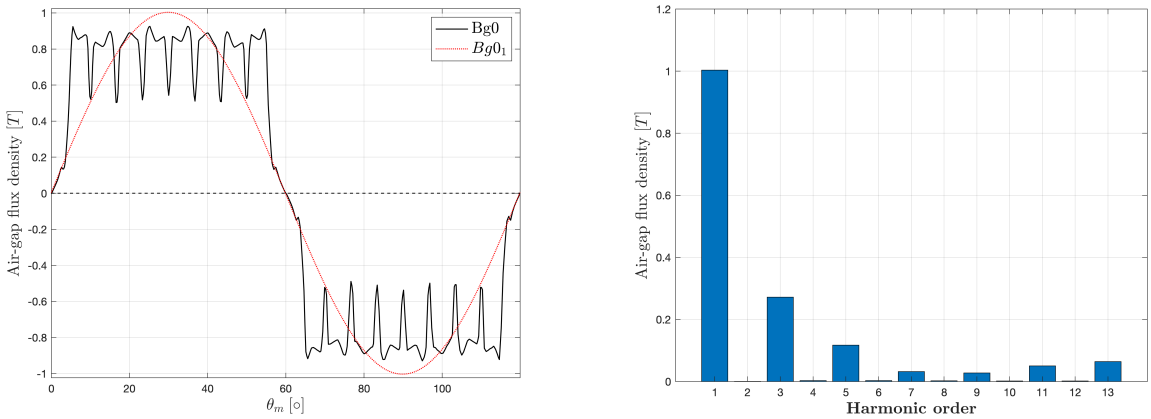

(a) Flux density plot

(b) Harmonic content

Figure 3.6: WR motor air-gap flux density

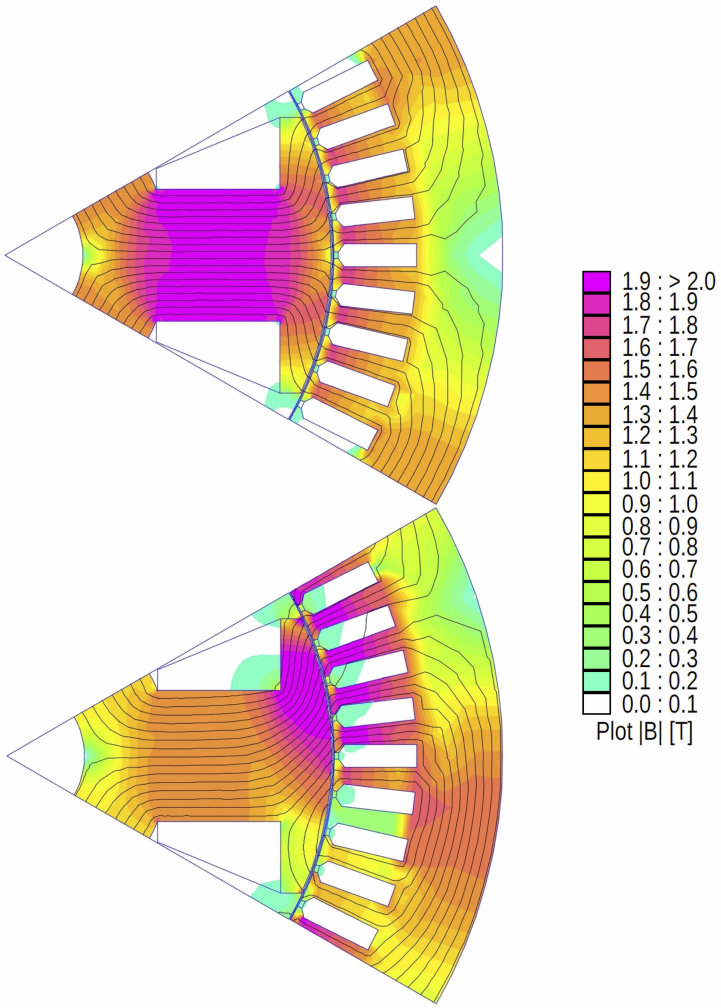

Figure 3.7: Flux density plot at no stator current state (up) vs peak torque point (down)

From Figure 3.7, it can be observed that at the peak torque point, the induction is quite high in the stator teeth (2T). If desired, it could be reduced by decreasing the excitation current. However, since this current is regulated and specifically reduced according to the operating point, I have decided to accept this not optimal condition.

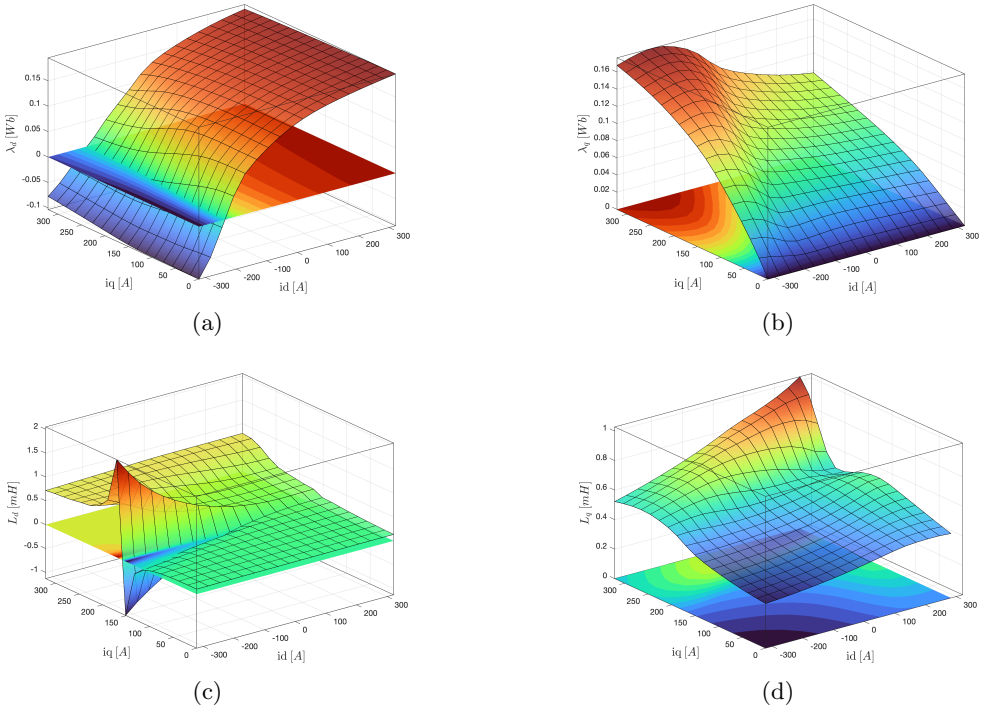

Figure 3.8: (100% Ie) Surface plots: (a) d-axis flux linkage, (b) q-axis flux linkage, (c) d-axis inductance, (d) q-axis inductance

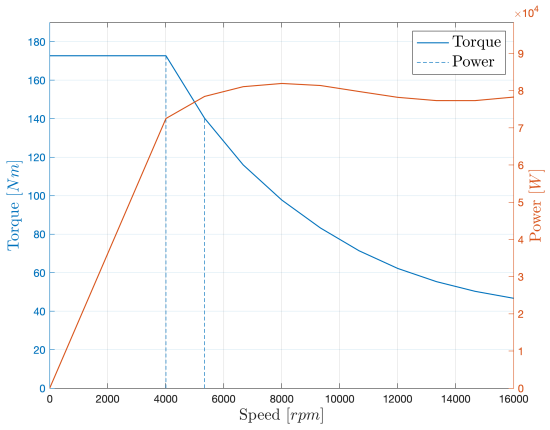

Figure 3.9: (100% Ie) Torque/Power vs Speed

In Fig. 3.9 the two dashed lines represent, respectively, the reference point and the transition speed between FW and MTPV. The machine in question is capable of generating a relatively constant mechanical power to the rotor.

Table 3.2: WR working point characteristics

Parameter	Symbol	Value	Unit
d-axis inductance	L_d	0.785	mH
q-axis inductance	L_q	0.759	mH
saiency	ξ	1.035	/
Base speed	n_b	4000	rpm
Max speed	n_{max}	16000	rpm
Max power	P_{max}	81.9	kW
Phase stator current	I_{peak}	292	A
Characteristic current	I_{ch}	194	A
DC Joule losses	PJs_{DC}	1682	W
Stator current density	J_s	8.33	A/mm^2
Rotor current density	J_r	6.25	A/mm^2

As mentioned earlier, by reducing the excitation current of the rotor, the center of the voltage ellipses shifts to the right (see Figure 3.10). Furthermore, it can be observed that the MTPA, FW, and MTPV trajectories need to be adjusted accordingly.

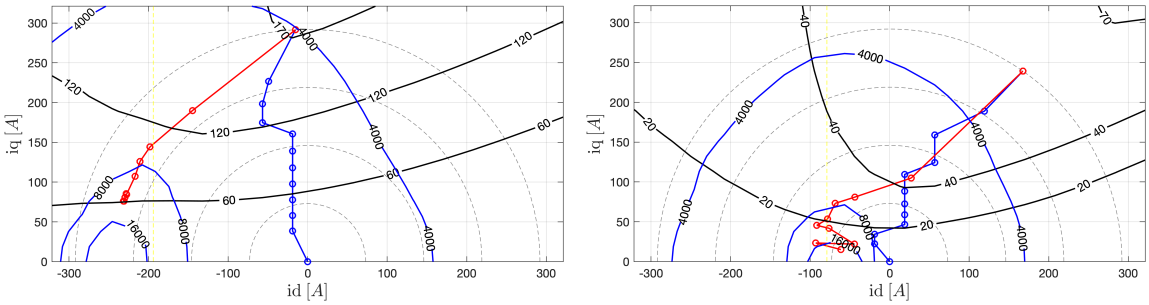

(a) 100% Ie (b) 30% Ie

Figure 3.10: MTPA (blue) and FW (red) trajectories

Furthermore, as illustrated in Figure 3.11, decreasing the excitation current of the rotor improves the power factor at high speeds (while deteriorating at low speeds).

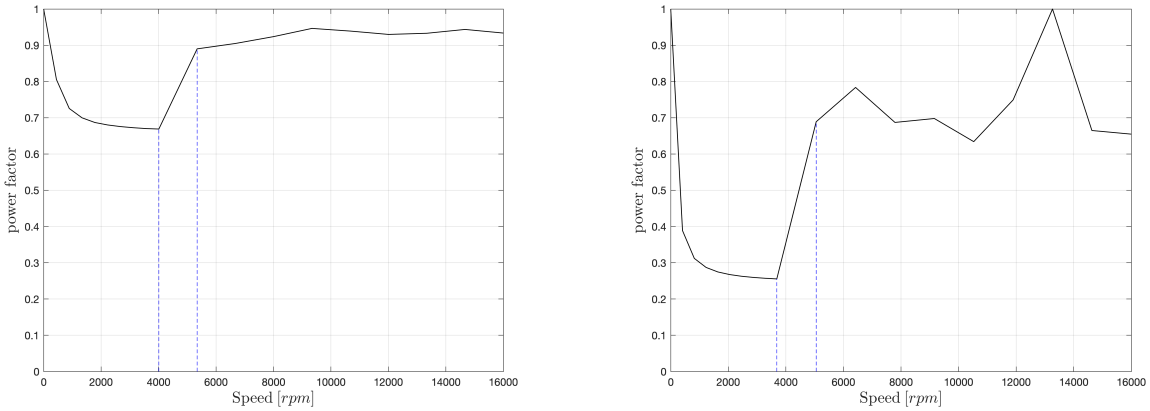

(a) 100% Ie (b) 30% Ie

Figure 3.11: Power factor

3.3 Excitation current control technique

As said before, to enhance motor performance at higher speeds, it is beneficial to reduce the rotor flux in relation to the speed. However, achieving this with a classical Interior Permanent Magnet motor is not feasible because the permanent magnets embedded in the rotor generate a fixed flux. On the contrary, if a WR motor is used, the rotor flux can be modified during the motor operation, so a control strategy for the excitation current must be developed. During FW operations the rotor flux is regulated to achieve the highest efficiency according to that speed and torque. Using the optimal rotor excitation current control, mixed with stator field weakening, above 86% effiency can be achieved in virtually all operation points above kneepoint, with a top efficiency greater then 93% for the machine. Various finite element simulations were carried out using different excitation current values, and by using a Matlab script, an efficiency map was generated on a torque-speed plane to identify the best excitation current value that optimizes the machine's performance.

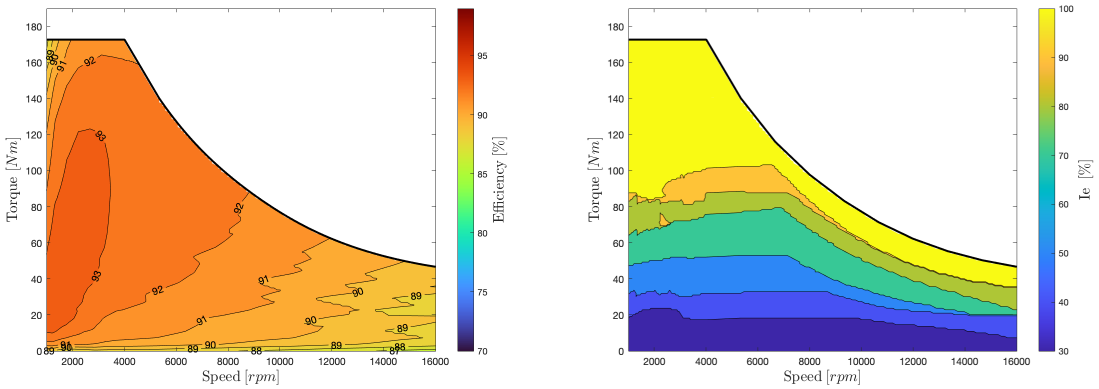

(a) (b)

Figure 3.12: Optimized efficiency map and excitation current

3.4 HEPM machine: analysis

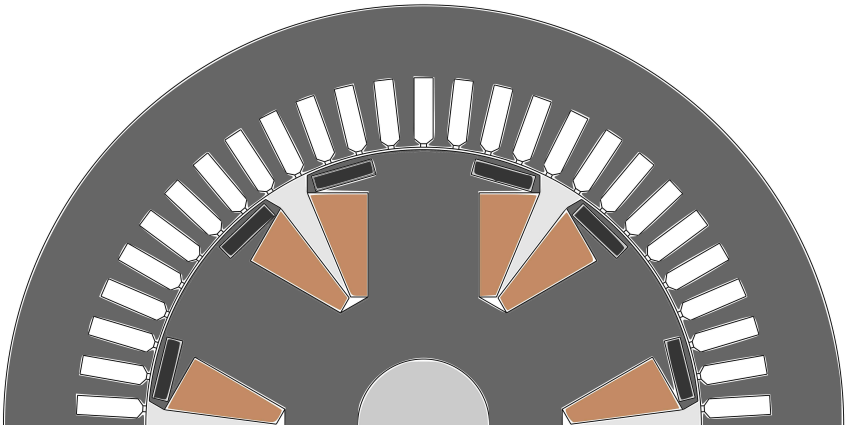

Figure 3.13: HEPM motor configuration

The Hybrid-Excitation Permanent-Magnet (HEPM) machine is a synchronous motor that combines permanent magnets (PMs) and excitation coils in its rotor. This unique design allows for a consistent magnetic flux at the machine's air gap generated by the PMs, while the excitation coils provide a controllable flux component.

Under normal conditions, the excitation current is used to augment the flux produced by the PMs, ensuring it remains constant and aligned with the desired machine performance. However, there are specific situations where adjustments to the flux may be necessary. During transient overload operations, there might be a requirement to increase the flux. This arises when the machine encounters temporary increases in load or power demand beyond its normal capacity. By increasing the flux, the machine can handle the overload momentarily without compromising its performance or causing damage. Conversely, Flux-Weakening (FW) actions involve operating the machine at speeds higher than its nominal speed. To achieve this, it is beneficial to decrease the flux. By reducing the flux, the machine can maintain stable operation at elevated speeds, preventing excessive power consumption or overheating issues that could occur if the flux remained constant.

One aspect that this study does not address is the structural resistance, which is undoubtedly reduced due to the presence of these magnets.

Table 3.3: Wound-rotor HEPM magnets parameters

Parameter	Symbol	Value	Unit
PM type	N55	-	-
PM thickness	tm	4.7	mm
PM length	lm	18	mm
PM tilt angle	α_{PM}	16	deg
PM total volume	V_{PM}	0.00013401	m^3

It employs only 45% of the magnet volume compared to the IPM, with the aim of enhancing torque density.

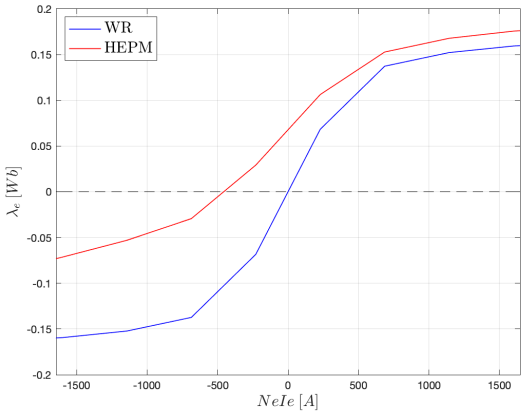

Figure 3.14: No-load flux linkage vs ampere turns

The no-load flux linkage (Fig. 3.14) is higher for HEPM than WR, along all the operating region. In particular, the additional contribute of the PM flux linkage is shown at $N_e I_e$ equal to 0A

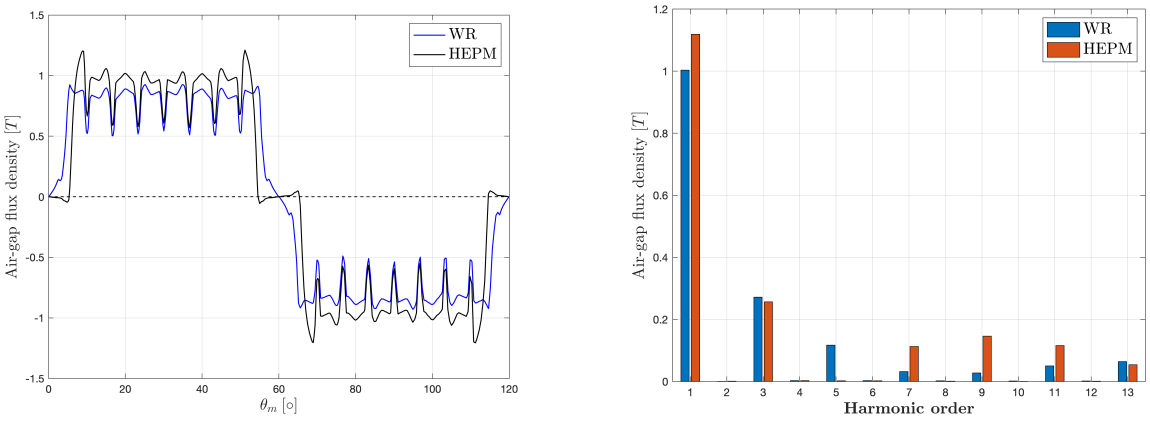

(a) Flux density plot

(b) Harmonic content

Figure 3.15: HEPM no-load motor air-gap flux density

The waveform of the flux density along the air-gap (Fig. 3.15) bears resemblance to the WR waveform, with a higher fundamental value. The fifth harmonic is almost eliminated, whereas higher-order harmonics are slightly more pronounced.

Regarding the magnetic inductions (Fig. 3.16), this machine exhibits a more saturated rotor compared to the WR.

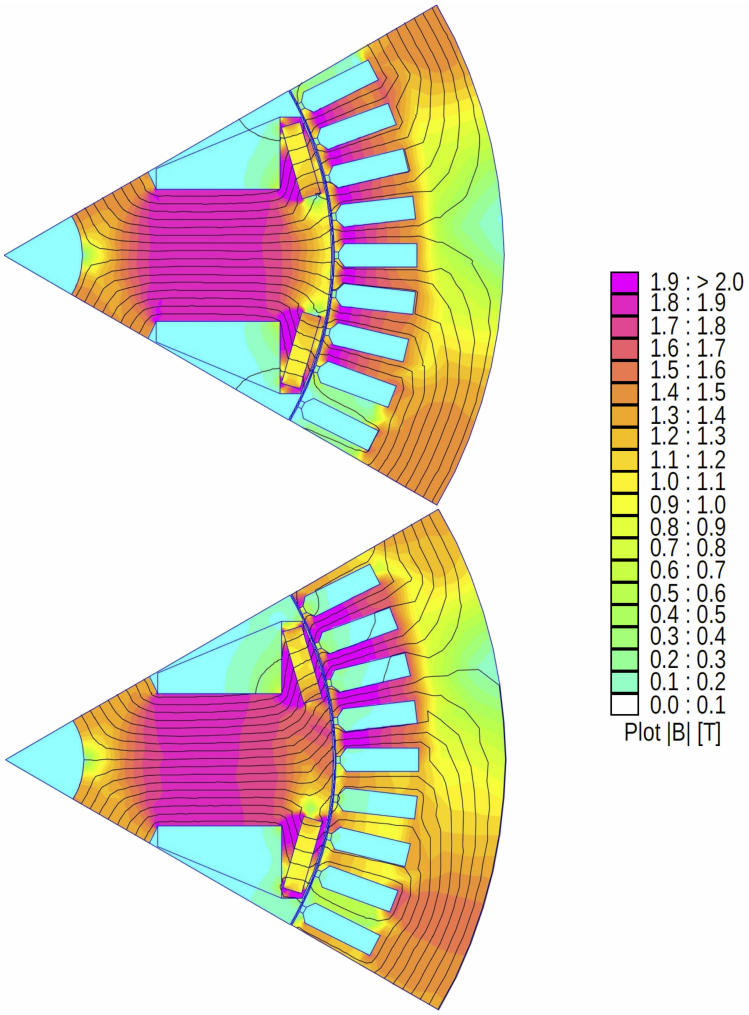

Figure 3.16: Flux density plot at no stator current state (up) vs peak torque point (down)

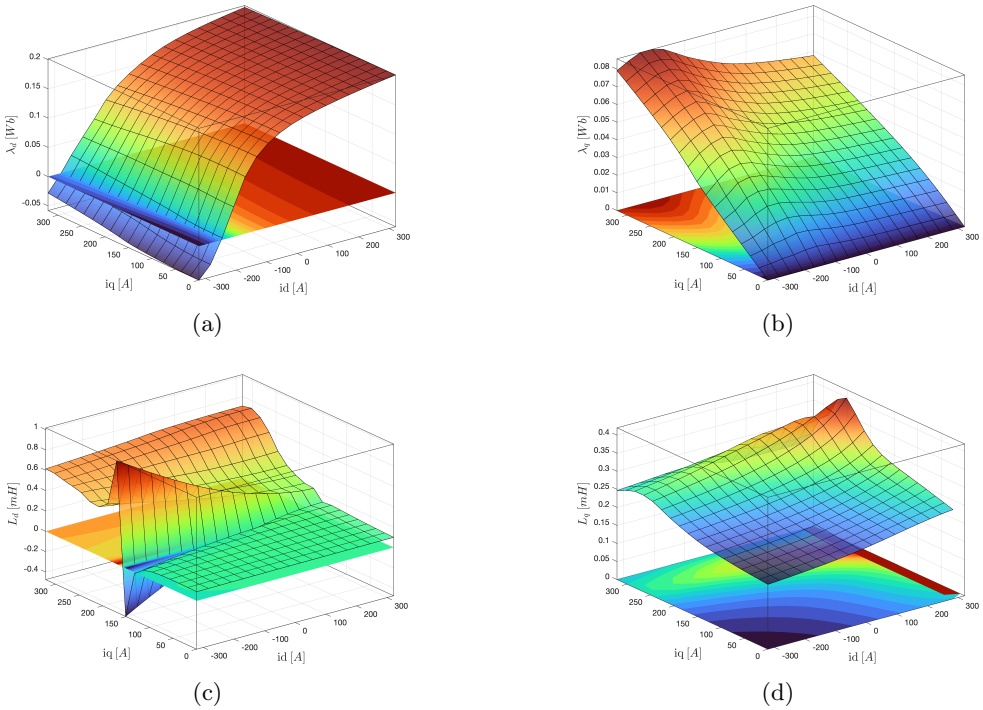

Figure 3.17: (100% Ie) Surface plots: (a) d-axis flux linkage, (b) q-axis flux linkage, (c) d-axis inductance, (d) q-axis inductance

When comparing the WR motor to this one, it is helpful to graph the torque, power, power factor, and efficiency against the rotor speed. These are depicted in Figure 3.18, where the benefits of magnet insertion in the rotor can be appreciated. In particular, the 20% increase in torque is highly appealing, especially in the field of electric traction. As for the efficiency map (Fig. 3.19), no significant differences are observed, except for a vertical elongation of the areas with efficiencies higher than 92%.

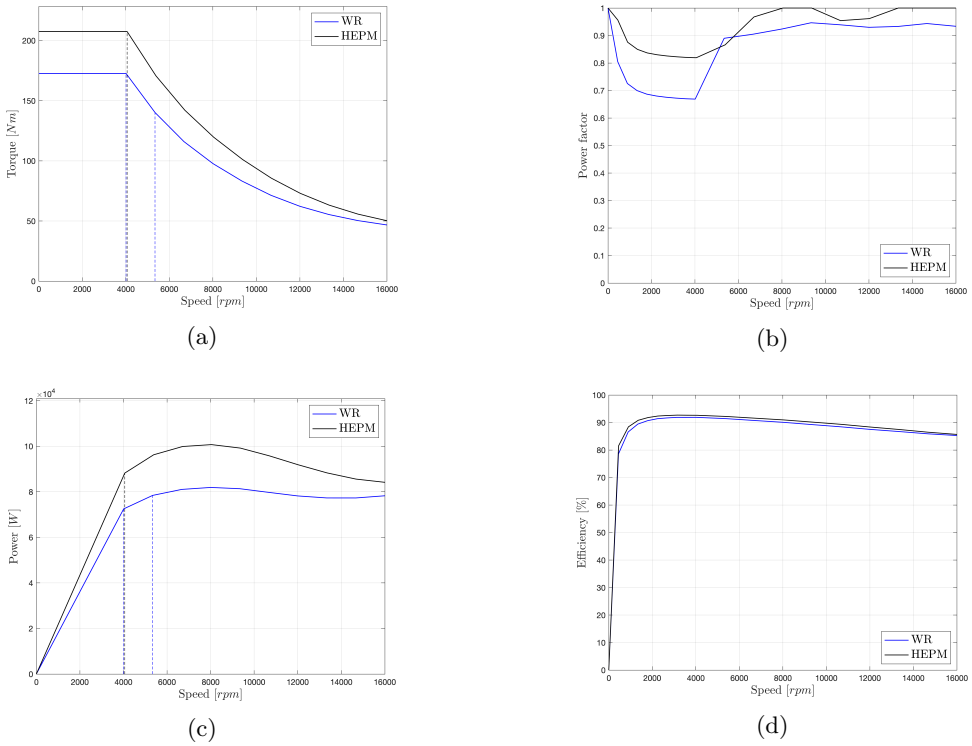

Figure 3.18: Torque, power factor, power and efficiency for WR and HEPM configurations: (a) torque, (b) power factor, (c) power, (d) efficiency

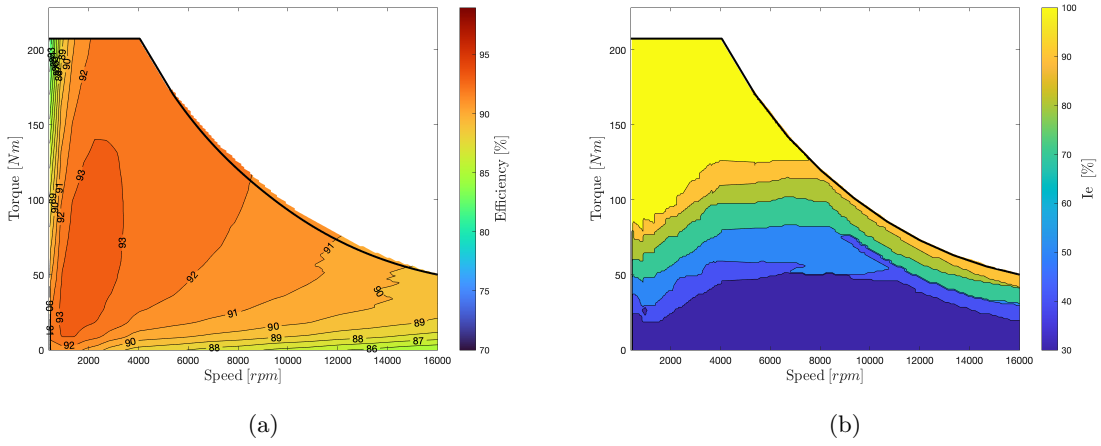

Figure 3.19: Optimized efficiency map and excitation current

Chapter 4

Synchronous reluctance machines

The main principle behind the REL motor is that its torque is solely generated by the rotor anisotropy. Therefore, it is crucial to maximize the saliency ratio for optimal performance. The rotor shares similarities with the interior permanent magnet rotor. However, it is designed with multiple barriers per pole.

Although the concept of the REL machine has been proposed several years ago, it has gained increasing popularity in various applications only recently. This is primarily due to its robustness, high efficiency, and the absence of excitation windings or permanent magnets. One significant advantage of the REL machine is the virtual absence of rotor losses, which leads to lower rotor temperatures.

However, if not properly designed, the REL machine can exhibit certain drawbacks, such as high torque ripple and a low power factor. Fortunately, researchers have extensively studied the design methodology in this field, focusing on reducing torque ripple and improving power factor. Consequently, the design process for REL machines is now well-established.

The key advantage of this technology lies in the rotor structure, which eliminates the need for excitation coils or permanent magnets. This feature makes REL machines highly cost-effective compared to other motor types.

In a REL machine, there are two distinct paths for the flux within the rotor. The first path, known as the d-axis path, consists of high-permeability rotor iron paths where the flux lines flow parallel to the flux barriers. The second path, known as the q-axis path, involves low-permeability regions where the flux lines have to cross the rotor flux barriers.

The rotor is specifically designed with multiple flux barriers to impede the flow of flux along the q-axis path, thereby achieving a high saliency ratio, which corresponds to a significant reluctance torque component. However, it is important to note that the rotor structure includes iron bridges that mechanically support the rotor parts and are present at the ends and sometimes in the middle of each barrier. These iron bridges allow a portion of the q-axis flux to flow through them, resulting in a reduction of torque.

For a given current, the flux linkage along the d-axis path is generally higher. However, the saturation of iron limits the maximum flux density along this path, especially at higher currents. It is worth mentioning that the inductances in the machine are not constant but vary with the stator current.

On the other hand, the flux linkage along the q-axis path is lower because it is constrained by the presence of the rotor flux barriers. However, this flux linkage remains nearly linear with the current. Near-zero currents, there is an observable change in the curve drop, which is attributed to the saturation of the iron bridges. This saturation affects the behavior of the q-axis flux linkage.

When a PM is introduced in the rotor flux–barriers, according to the reference frame defined above, it produces a negative flux linkage along the q-axis. The inductance Ld (which is related to the main flux of the machine) corresponds to the magnetizing inductance. The inductance Lq is

quite low, since it corresponds to the flux obstructed by the flux barriers. The ratio between d-axis and q-axis inductance defines the rotor saliency ξ, that is, $\xi = Ld/Lq$. This notation is in contrast to the one used earlier for the interior permanent magnet motor.

Two reluctance motor configurations are shown in Figure 4.1, along with the commonly used notation for the d- and the q-axis.

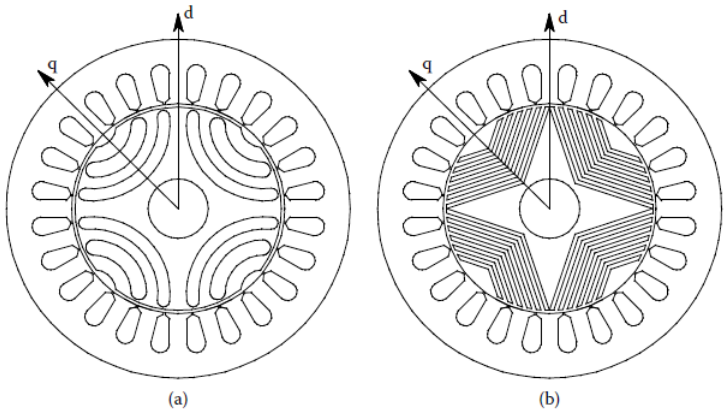

Figure 4.1: (a): transversally laminated rotor, (b): axially laminated rotor [4]

4.1 Motor model and operating condition

4.1.1 Saturation effects

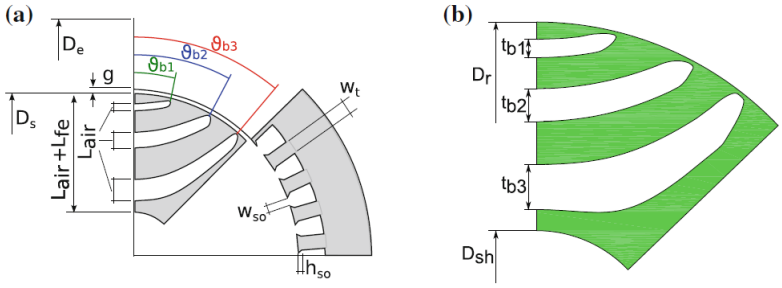

Figure 4.2: Motor geometry for the computation of coefficient k_{air} [14]

The influence of iron saturation on machine performance is examined by varying the thickness of the flux-barriers. Referring to Fig. 4.2 the coefficient k_{air} is defined as:

$$k_{air} = \frac{\sum_i t_{bi}}{(D_r - D_{sh})/2} \tag{4.1}$$

The thicknesses of the flux-barriers, denoted as t_{bi}, are related to the external rotor diameter (D_r) and shaft diameter (D_{sh}). The coefficient k_{air} is selected based on the stator geometry. By increasing the saturation level through the enlargement of flux-barrier thickness (i.e., increasing k_{air}), the flux density in the rotor increases. However, the phenomenon is reversed in the stator, where the flux density amplitude decreases due to saturation. The coefficient k_{air} is chosen based on the stator geometry, and a corresponding coefficient $k_{air,s}$ can be defined specifically for the

stator geometry as follows:

$$k_{air,s} = \frac{p_s - w_t}{p_s} \tag{4.2}$$

It is clear that for a well-saturated machine, the rotor's k_{air} should closely match the stator's $k_{air,s}$. Additionally, to minimize iron losses, the stator's $k_{air,s}$ should be slightly lower than the rotor's k_{air}.

4.1.2 Torque production

The expression of the torque of a REL machine can be computed as 4.3, which shows how strictly it is correlated to the $d-q$ flux linkages.

$$T = \frac{3}{2}p(\Lambda_d I_q - \Lambda_q I_d) + \frac{dW_{mc}(i_d, i_q, \theta_m)}{d\theta_m} \tag{4.3}$$

W_{mc} is the magnetic coenergy that is a function of i_d, i_q and θ_m. The $d-q$ flux linkages exhibit a correlation with the k_{air} coefficient, as both decrease with an increase in k_{air} due to iron saturation, particularly at higher currents. Consequently, the torque and power decrease as k_{air} increases. The thickness of the flux-barriers also affects torque ripple, where in higher rotor saturation leads to a decrease in the amplitude of higher torque harmonics.

The primary limitation of reluctance machines is the presence of significant torque ripple caused by the interaction between the stator's magnetomotive force and the rotor structure. By employing a rotor design consisting of multiple flux barriers per pole, the rotor geometry strongly impacts the machine's performance, affecting both the average torque and torque ripple. Consequently, optimization efforts are often necessary to determine the ideal rotor geometry that can yield both high and smooth torque characteristics.

4.1.3 Flux-barriers and iron channels design

In order to achieve a high average torque value and reduce ripple, special attention is given to the design of the rotor geometry. The two most commonly used topologies are called fluid and segmented, and we will focus on analyzing the fluid one.

The design of the fluid flux-barriers follows specific criteria, aligning their edges with predetermined flux lines that would be present in the case of a d-axis magnetization of a solid rotor. This design strategy helps minimize distortion in the d-axis flux lines and effectively block the q-axis ones, resulting in a beneficial effect on the rotor's anisotropy. The following figure illustrates an example of how the flux barriers of a fluid rotor follow the flux lines obtained by supplying the stator winding with a d-axis current. The following motor will be analyzed in a subsequent chapter.

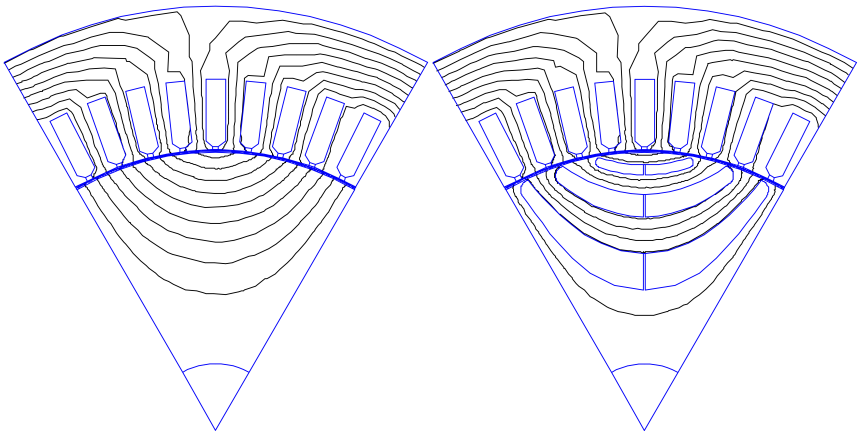

Figure 4.3: d-Axis flux lines and relative flux-barriers geometry

4.1.4 Power factor

A drawback of the REL motor is its relatively low power factor. The vector diagram in Figure 4.4 illustrates that the voltage vector leads the current vector, resulting in a relatively high power factor angle.

A higher rotor saliency in the REL motor design contributes to a better power factor because it enables a better separation of the flux produced by the d-axis current and the q-axis current. This separation reduces the interaction between the two currents, leading to a smaller reactive power component and a higher power factor. In addition, the introduction of permanent magnets (PM) along the negative q-axis helps compensate for the negative flux $L_{\mathrm{q}}I_q$. As depicted in the vector diagram shown in Figure 4.4, the PM flux linkage causes the flux linkage vector to be out of phase with the current vector. This rotation of the flux linkage vector toward the current vector leads to an increase in power factor.

Consequently, the PMaREL motor can achieve a given nominal mechanical power with a lower Volt-Ampere rating, thanks to the improved power factor resulting from the inclusion of the PM flux linkage.

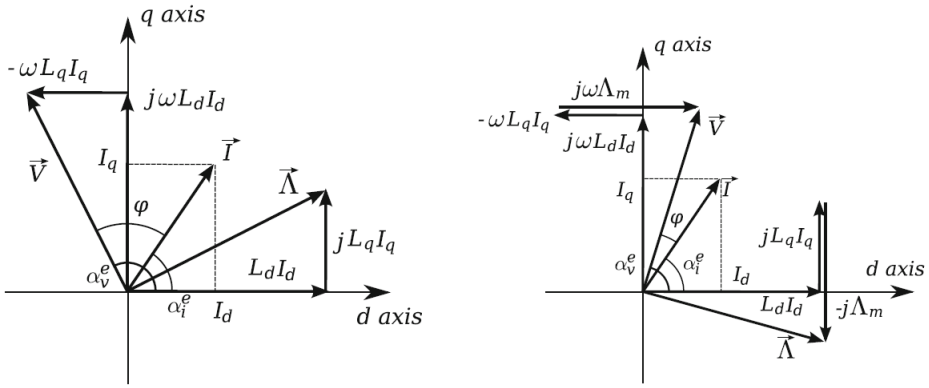

Figure 4.4: Vector diagram of the REL (left) and PMaREL (right) motor. [14]

4.2 REL machine: analysis

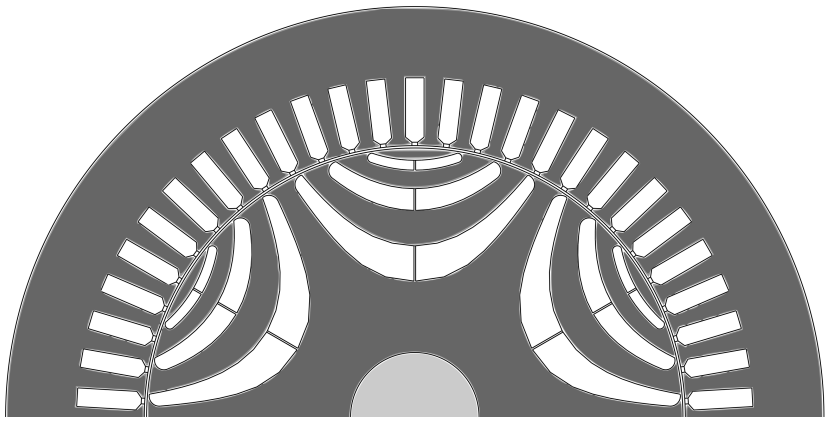

Figure 4.5: REL motor configuration

To represent the category of reluctance motors, employing the same stator as the other 6-pole machines in this study, I designed a rotor with a three flux barrier design featuring fluid geometry. My aim was to optimize the coupling of the coefficients k_{air} and $k_{air,s}$.

Table 4.1: REL geometry parameters

Parameter	Symbol	Value	Unit
Stator slots	Q_s	54	-
Pole number	2p	6	-
Outer diameter	D_e	242	mm
Inner diameter	D_i	160	mm
Stack length	L_{stk}	132	mm
Air gap	g	0.7	mm
Shaft diameter	D_{sh}	38	mm
Back-iron heigth	h_{bi}	21	mm
Slot heigth	h_s	20	mm
Open slot width	w_{so}	1.7	mm
Wed heigth	h_{wed}	1.5	mm
Tooth width	w_t	4.97	mm
Slot width	w_s	5.5	mm
Stator fill factor	k_{fill}	0.65	-
Stator slot area	S_{slot}	101.65	mm^2
Stator conductors in slot	n_c	8	-
Parallel stator paths	n_{pp}	3	-
Excitation turns	n_{cs}	2.666	-

In Figure 4.6, we can observe how the saturated regions are localized in the stator yoke (1.4T), the teeth (1.9T), and along the edges of the flux barriers.

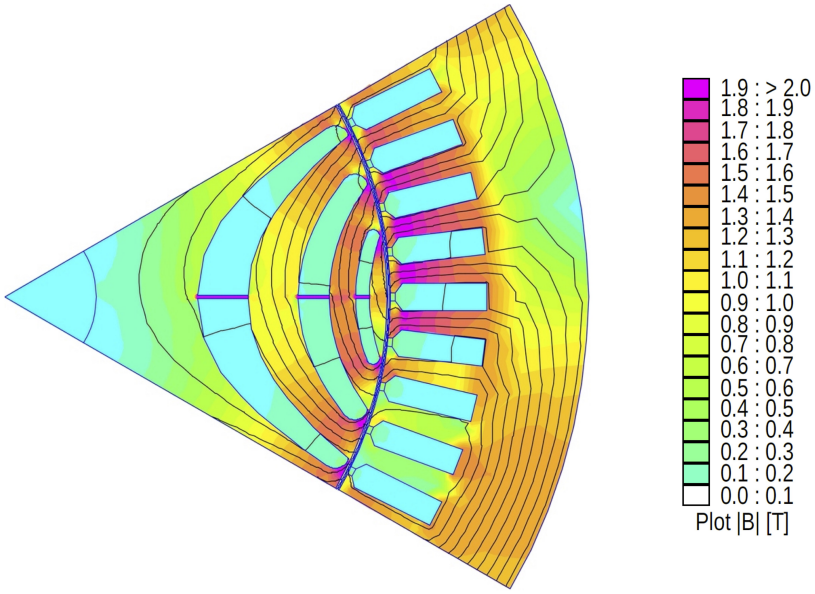

Figure 4.6: Flux density plot at peak torque point

Typically, reluctance motors demonstrate relatively low values of Constant Power Speed Range. From a design perspective, this low CPSR is associated with the presence of radial and tangential ribs. These ribs increase the leakage flux, thereby raising the inductance along the q-axis (Lq) and reducing the saliency ratio (ξ) during field weakening operation, where the voltage is limited to its rated value. The output power characteristic of the REL machine relies on the value of ξ. Therefore, achieving a higher CPSR in field weakening conditions is dependent on increasing ξ. Consequently, it can be stated that in a conventional reluctance motor, maintaining a constant peak power during field weakening operation at higher speeds is challenging or even impossible due to the mentioned physical reason [13]. This can be seen in Figure 4.7.

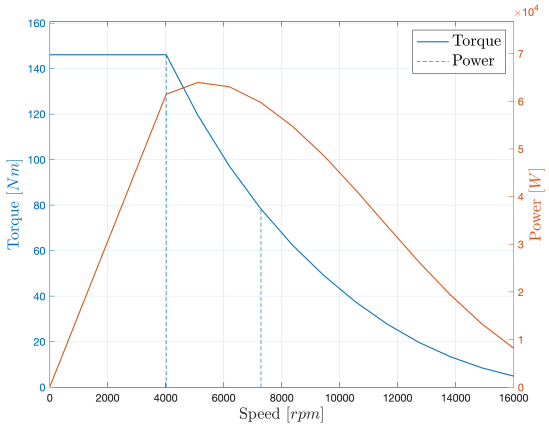

Figure 4.7: Torque/Power vs Speed

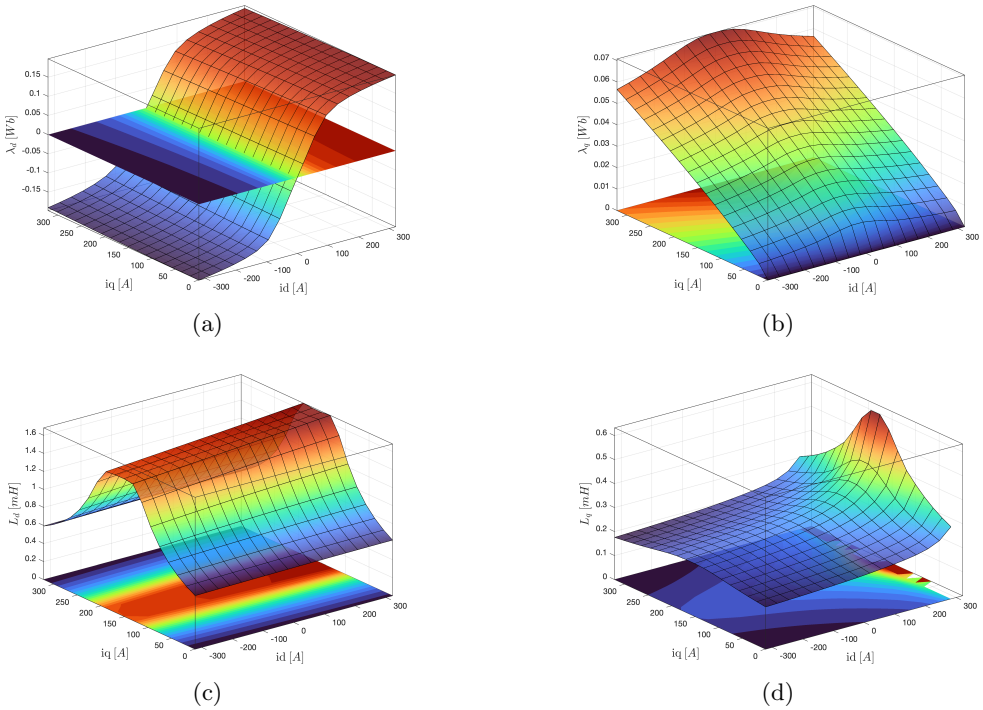

Figure 4.8: Surface plots: (a) d-axis flux linkage, (b) q-axis flux linkage, (c) d-axis inductance, (d) q-axis inductance

As anticipated, the power factor is lower compared to the machines studied so far. At the base point, it is only 0.62, as shown in Figure 4.9.

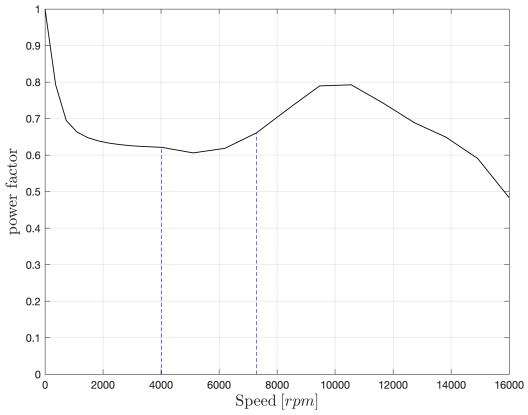

Figure 4.9: Power factor versus speed

This type of machine typically operates in the first quadrant of the idq plane. In Figure 4.10, we can observe the trajectory of MTPA (Maximum Torque per Ampere), FW (Field Weakening), and MTPV (Maximum Torque per Voltage) up to the 16000rpm ellipse.

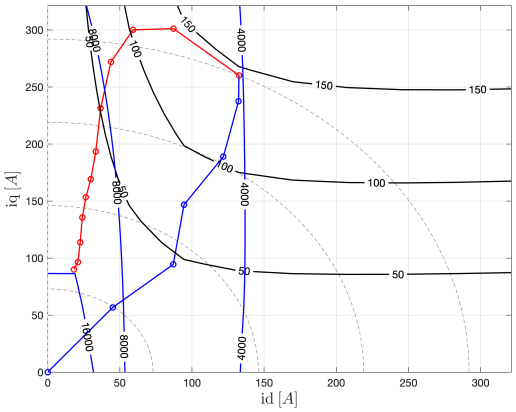

Figure 4.10: MTPA (blue) and FW (red) trajectories

Regarding the efficiency map (Fig. 4.11), it exhibits lower values compared to other machines. However, for the majority of the speed range, it is possible to operate with an efficiency greater than 90%.

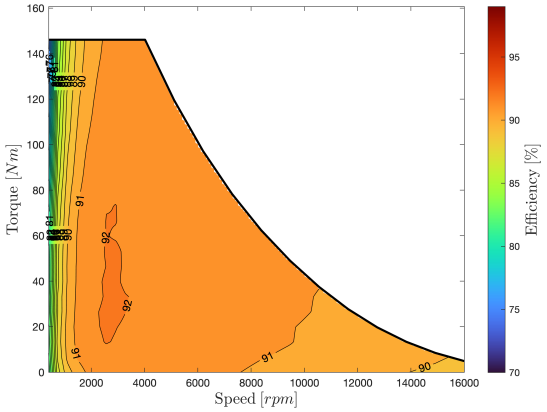

Figure 4.11: Torque versus speed efficiency map

4.3 PMaREL machine: analysis

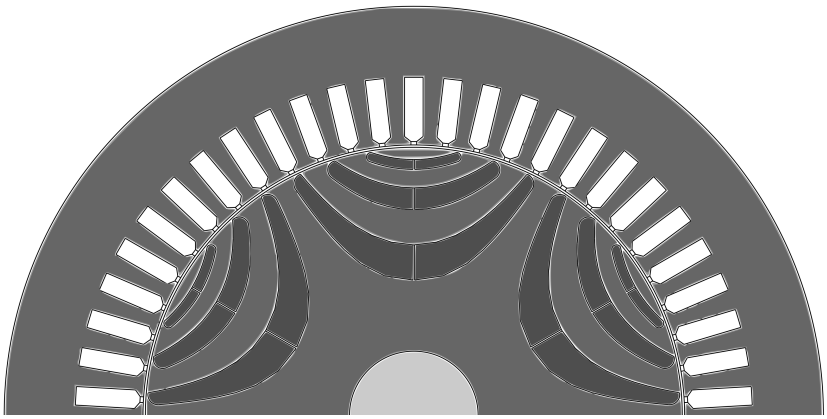

Figure 4.12: PMaREL motor configuration

The Permanent Magnet assisted Synchronous Reluctance (PMaREL) machine is a well-known solution for addressing the power capability limitation of the Synchronous Reluctance machine. It achieves this by incorporating a small Permanent Magnet flux contribution. The choice of design and economic strategies determines whether rare earth PMs or low magnetic energy ferrites are used to generate the excitation flux. Both options allow the PMaREL machine to remain cost-effective compared to the traditional rare-earth-based permanent magnet synchronous machine. In recent years, the preference has shifted towards the latter option to mitigate risks associated with fluctuations in rare-earth materials' costs. The PMaREL machine is widely adopted in various applications, including home appliances, spindle systems, and automotive applications.

The key design factors for the PMaREL machine are the geometry of the flux barriers and PM compensation. While these aspects are interconnected, the flux barrier geometry primarily influences average torque and torque ripple, whereas PM compensation affects high-speed power capability. To simplify rotor geometry and manufacturing costs, rectangular PMs are commonly used. However, this design choice significantly limits machine performance when high PM compensation is required because only a small portion of the effective flux-barriers cross-sectional area can be filled with PMs.

To overcome these limitations, Bonded Magnets (BMs) offer a viable solution as they can be easily shaped or directly injected into the flux barriers. BMs enable the realization of a PMaREL rotor and provide a higher amount of PM materials compared to the conventional approach. BMs are composed of a mixture of magnetic powder and a polymeric binder. The choice of magnetic powder can be hard ferrite, NdFeB, or SmCo, while the binders depend on the molding process used. Polyamide (PA) is commonly used for injection molding, while thermoset resins are used for compression molding. Both molding technologies can produce BMs in complex shapes. Additionally, the magnetic properties of BMs can be adjusted by varying the percentage of the plastic binder. NdFeB BMs exhibit superior magnetic characteristics compared to ferrites, particularly in terms of high intrinsic coercivity.

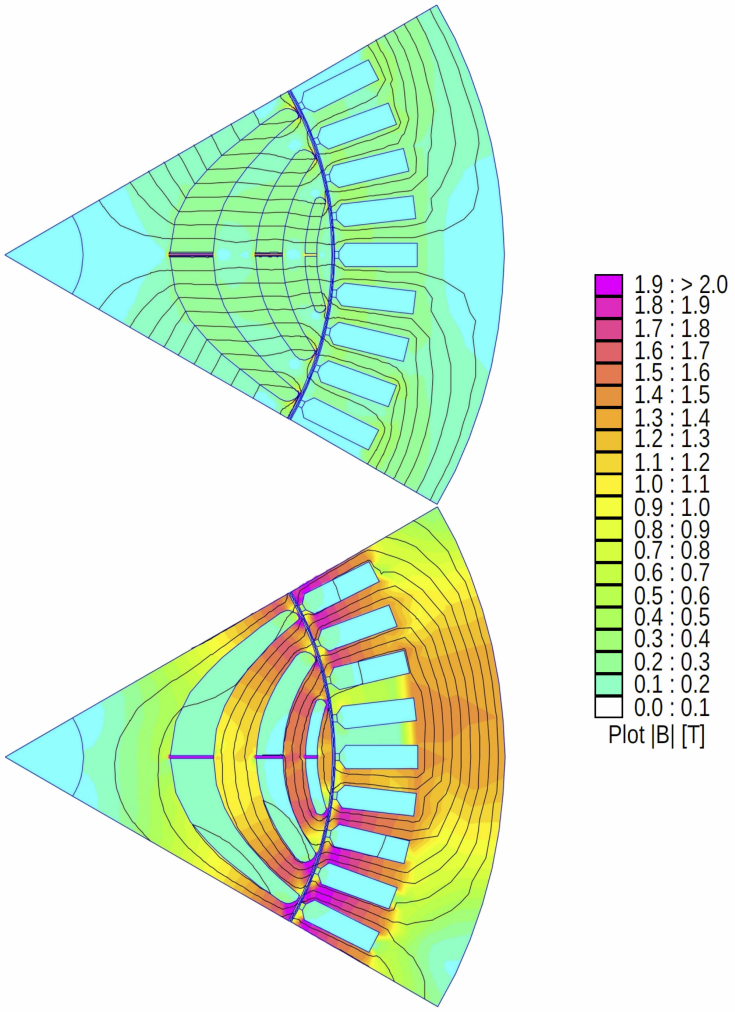

Figure 4.13: Flux density plot at no current state (up) vs peak torque point (down)

From Figure 4.13, we can observe how the ferrite magnets generate significantly lower inductions compared to the NdFeB magnets when operating at no current state. On the other hand, under load conditions, the most magnetically saturated parts appear to be the stator teeth and the crown. Below (see Fig. 4.14), a comparison between REL and PMaREL motors is presented. Specifically, it can be observed that the addition of magnets has increased the torque/power output and improved the power factor across the entire operating range.

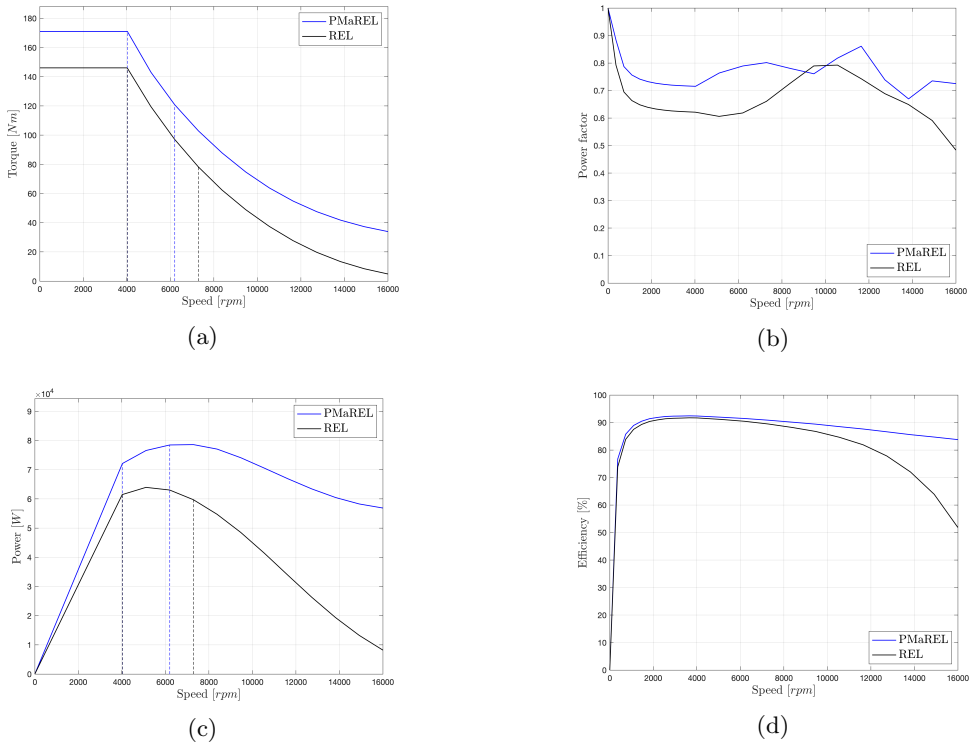

Figure 4.14: Torque, power factor, power and efficiency for PMaREL and REL configurations: (a) torque, (b) power factor, (c) power, (d) efficiency

The addition of magnets has also enhanced the machine's efficiency map, expanding the region with efficiency greater than 92% and reaching a maximum efficiency of 93% (Fig. 4.15).

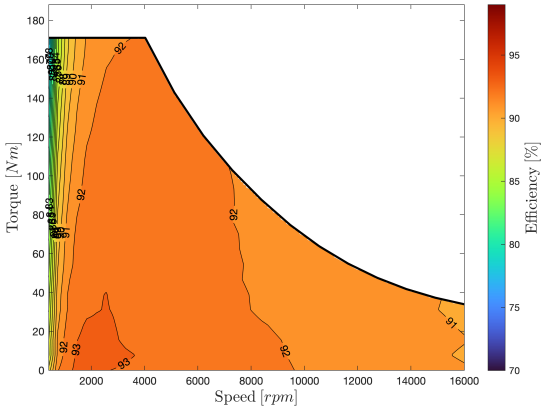

Figure 4.15: Torque versus speed efficiency map

Chapter 5

Thermal analysis

It is often necessary to perform heat transfer simulation in electrical machines during the design phase to anticipate temperature levels. The temperatures in the machine impact material selection and overall cost and has consistently been the primary factor affecting the performance limitations of electrical machines. Since these machines are intricate, striking a balance between precision and computational expenses becomes crucial. The model utilized consists of a network comprising thermal resistors and capacitors, which are established using the T-nodal method. Numerous components within synchronous machines are particularly susceptible to temperature variations, such as the slot insulators and magnets. To address this constraint, researchers have dedicated efforts to developing models that can precisely predict temperatures within these machines. The two predominant methods employed for this purpose are the Finite Element Method (FEM) and the lumped parameter method. In permanent magnet synchronous machines, there exists a potential hazard of irreversible demagnetization of the magnets. As the temperature of the magnets increases, their magnetization weakens, leading to a reduction in torque output. To compensate for this effect and maintain a consistent torque level, the current is augmented. Consequently, this results in increased copper losses in the stator slot. Therefore, in such machines, copper losses are influenced not only by the temperature of the copper but also by the temperature of the magnets [8].

5.1 Lumped parameter thermal network

The process begins with the utilization of an electrical analogy:

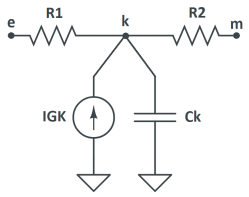

Figure 5.1: T-node with heat source and thermal capacity

Referring to figure 5.1, we can write the Kirchhoff equation at node k:

$$\frac{V_k(i) - V_e(i)}{R_1} + \frac{V_k(i) - V_m(i)}{R_2} = I_{GK} - \frac{C_k}{\Delta_t}[V_k(i) - V_k(i-1)] \tag{5.1}$$

The equation 5.1 can be rewritten as:

$$\begin{aligned} transient &: V_k(i)(\frac{1}{R_1} + \frac{1}{R_2} + \frac{C_k}{\Delta_t}) + V_e(i)(-\frac{1}{R_1}) + V_m(i)(-\frac{1}{R_2}) = I_{GK} + \frac{C_k}{\Delta_t}V_k(i-1) \\ steady - state &: V_k(i)(\frac{1}{R_1} + \frac{1}{R_2}) + V_e(i)(-\frac{1}{R_1}) + V_m(i)(-\frac{1}{R_2}) = I_{GK} \end{aligned} \tag{5.2}$$

So to solve a thermal network made of various T-nodes:

$$\begin{aligned} transient &: \vec{V}(i) = [A]^{-1}(\vec{I}(i) + \frac{\vec{C}}{\Delta_t}\vec{V}(i-1)) \\ steady - state &: \vec{V}(i) = [A]^{-1}\vec{I}(i) \end{aligned} \tag{5.3}$$

Where A is the thermal conductance matrix and the vector $\vec{V}$ contains the temperatures of each node. The calculation of thermal resistances and capacitances is omitted in this study.

5.1.1 Hairpin thermal network

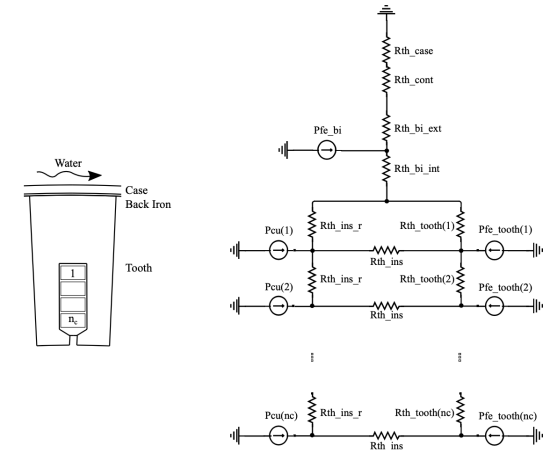

(a) *Sketch of one slot.* (b) *Thermal network.*

Figure 5.2: Implemented thermal network to determine the stator temperature in different working points.

Figure 5.2 shows the thermal network used in the simulation. The thermal capacities are not depicted in the figure, but I have accounted for one for each node. The model considers the uneven distribution of Joule losses within the slot due to high frequency. As a result, Joule losses are calculated separately for each wire in the slot and are used as input for the thermal analysis. The thermal calculations use the losses computed in the previous section as input. The analytical model is validated against the numerical one based on the average copper temperature within the slot.

5.1.2 Wound Rotor: rotor thermal network

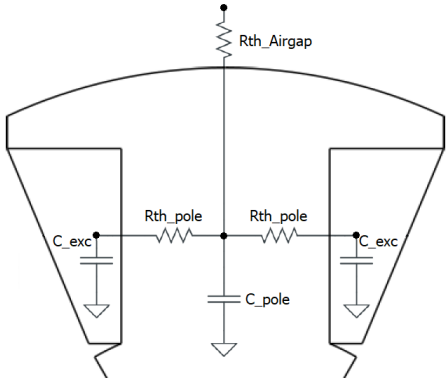

Figure 5.3: Implemented thermal network to determine the rotor temperature in different working points.

Since I didn't include rotor cooling in this study, in order to consider the worst-case scenario, I implemented a very basic thermal network. This approach can prove accurate both in steady-state conditions, where the entire rotor reaches almost the same temperature, and during transient overload, where the heat exchange of the windings behaves as if it were adiabatic.

5.2 Cooling system

All the machines have been designed considering liquid cooling of the external casing. This approach is typical for electric machines in traction applications, in fact it can be seen in vehicles such as the Nissan Leaf and BMW i3. The finite element model is represented in the next section.

Afterward, I assess the steady-state rated points by comparing the numerical values obtained with the analytical ones, and the transient overload points (analytical) only to ensure that Class F is respected within 30 seconds.

The thermal class H allows for a maximum temperature rise of 140°C.

5.3 Finite element method

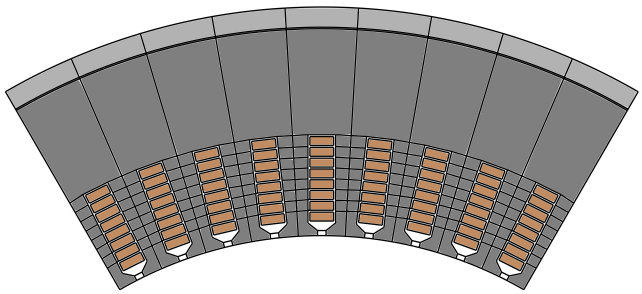

Figure 5.4: FEM model of a stator portion

Figure 5.4 illustrates the representation of a stator portion in the FEMM software, modelled to match the lumped network. The outermost layer, which is made of aluminum, corresponds to the aluminum casing of the motor that allows cooling water to flow through it. A $0.03mm$ layer of still air exists between the motor and the casing. To prevent a very small mesh size, this layer is represented in the model as a 2 mm layer with a thermal conductivity of $0.2W/(mK)$, which is 10 times greater than that of stagnant air ($0.02W/(mK)$). The copper losses are applied conductor by conductor, taking into account a higher density near the slot opening. The iron losses are divided between the back-iron and the teeth. A convection boundary condition of $1000W/(m^2K)$ was applied to the outer diameter to represent liquid cooling.

5.4 Results

The same procedure was applied to all five machines, but here I will specifically report the results obtained with the IPM and WR motors. Also, the most significant results for all the machines are presented in Table 6.1.

5.4.1 Base speed rated point

IPM

Table 5.1: IPM input parameters

Parameter	Symbol	Value	Unit
Shaft speed	n	4000	rpm
Torque	T	200.85	Nm
Stator current density	J_s	9.7	A/mm^2
Back-iron losses	Pfe_{bi}	361.348	W
Teeth iron losses	Pfe_t	342.94	W
Stator Joule losses	P_{Js}	1815.2	W

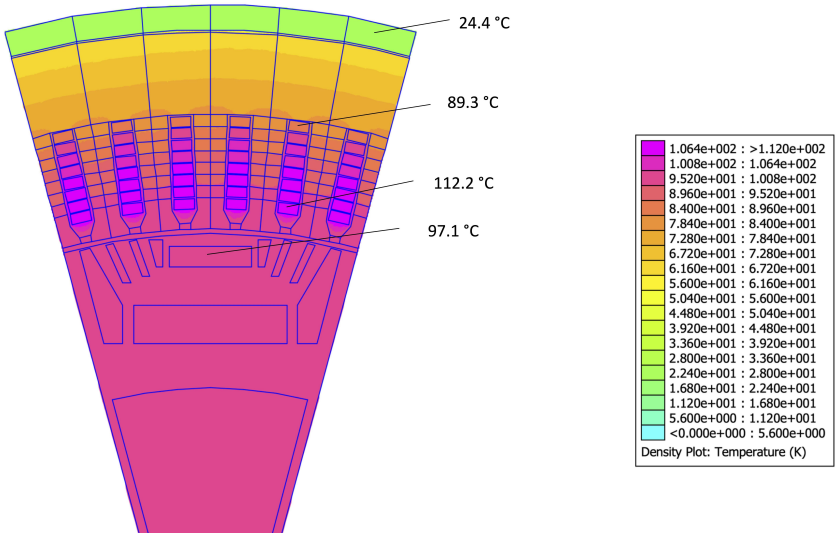

Figure 5.5: Temperature rise map of the IPM motor at 4000 rpm

Below, I compare the average slot temperatures obtained using the lumped thermal network and the FEM simulation, respectively.

- lumped thermal network: 103.16°C
- FEM: 104.56°C

WR

Table 5.2: WR input parameters

Parameter	Symbol	Value	Unit
Shaft speed	n	4000	rpm
Torque	T	172.68	Nm
Stator current density	J_s	8.33	A/mm^2
Rotor current density	J_r	6.25	A/mm^2
Excitation current percentage	$I_{e\%}$	100	%
Back-iron losses	Pfe_{bi}	324.39	W
Teeth iron losses	Pfe_t	210.29	W
Stator Joule losses	P_{Js}	1721.8	W
Rotor Joule losses	P_{ecc}	157.69	W

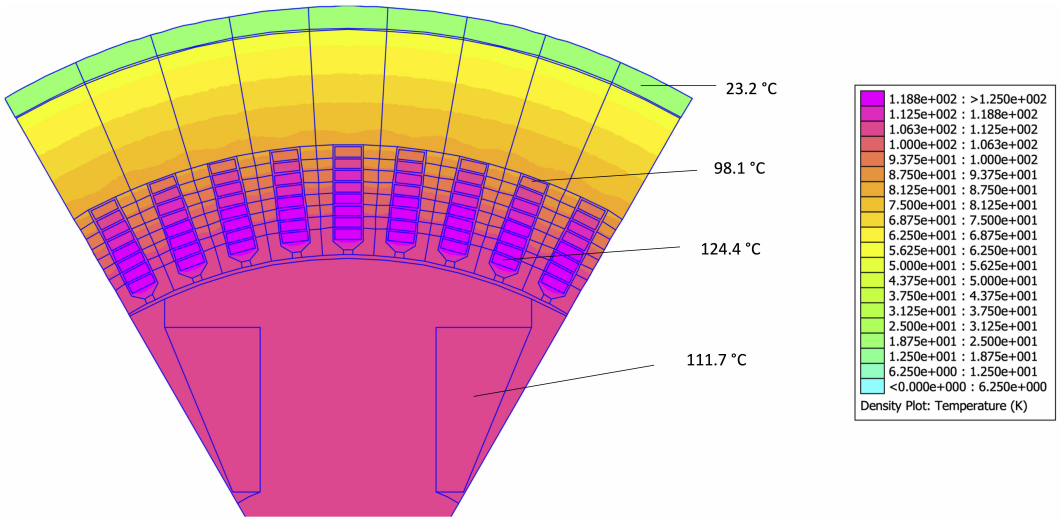

Figure 5.6: Temperature rise map of the WR motor at 4000 rpm

Below, I compare the average slot temperatures obtained using the lumped thermal network and the FEM simulation, respectively.

- lumped thermal network: 108.29°C
- FEM: 115.9.°C

5.4.2 Base speed overload point

By using a stator current density of $J_s = 20A/mm^2$, it can be seen whether the temperature of the conductors in the IPM and WR motors remains below the limit set by the H thermal class for a duration of 30 seconds (assuming an initial temperature of 50°C). It should be noted that the WR motor also allows for overload of the rotor excitation windings, resulting in a greater torque production (Fig. 5.7).

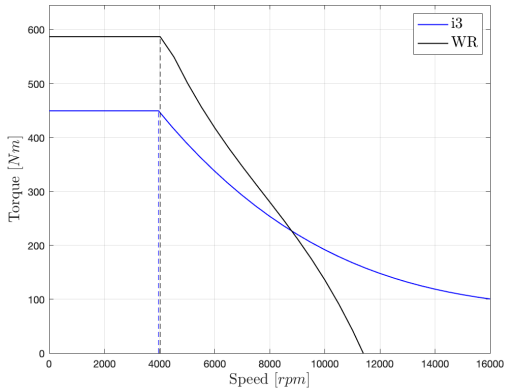

Figure 5.7: Overload torque production

- IPM

Table 5.3: IPM Input parameters

Parameter	Symbol	Value	Unit
Shaft speed	n	4000	rpm
Torque	T	450	Nm
Stator current density	J_s	20	A/mm^2
Back-iron losses	Pfe_{bi}	550.74	W
Teeth iron losses	Pfe_t	509.04	W
Stator Joule losses	P_{Js}	7764.8	W

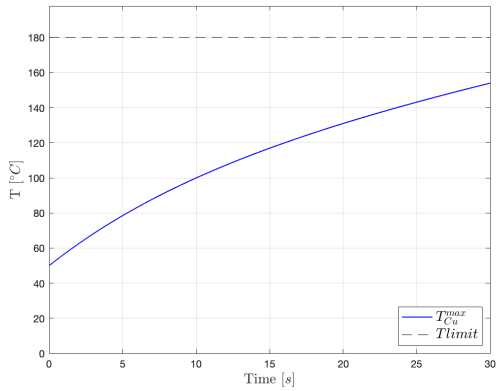

Figure 5.8: Temperature transient

- WR

Table 5.4: WR input parameters

Parameter	Symbol	Value	Unit
Shaft speed	n	4000	rpm
Torque	T	587	Nm
Stator current density	J_s	20	A/mm^2
Rotor current density	J_r	30	A/mm^2
Back-iron losses	Pfe_{bi}	387.03	W
Teeth iron losses	Pfe_t	241.34	W
Stator Joule losses	P_{Js}	10008	W
Rotor Joule losses	P_{ecc}	7921.2	W

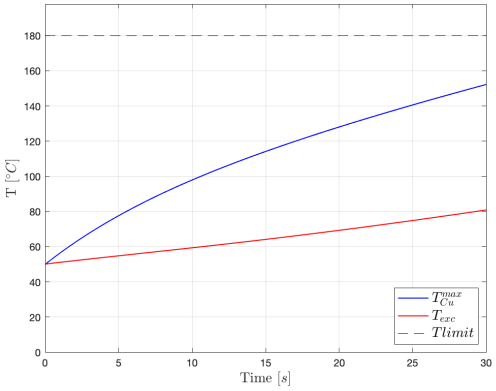

Figure 5.9: Temperature transient

Chapter 6

Machines comparison

Comparisons between different motor topologies are always very delicate to make. I chose to keep the external dimensions the same for all machines, including the diameter and stack length. For the four 6-pole machines, since they have the same number of slots, I considered an identical winding arrangement to make the comparison more equitable. Additionally, I selected the voltage and current limits in accordance with the characteristics of the BMW i3 inverter. I am asking a base speed of 4000 rpm and a maximum speed of 16000 rpm, however the maximum speed declared by BMW for their IPM motor is only 11400 rpm. It should be noted that the IPM motor has 12 poles, while the other machines have 6 poles. Therefore, I had to reduce the internal diameter of the 6-pole machines' stator to contain inductions in the stator teeth and back iron. When considering a fixed stator outside diameter, employing a higher number of poles in a motor design leads to an increased rotor volume and, to a lesser extent, electric loading. Consequently, the motor exhibits an enhanced capability for generating output torque. On the other hand, utilizing a decreased rotor diameter offers the benefit of reduced rotor inertia, leading to quicker dynamic response. Additionally, it results in diminished mechanical stresses on the rotor during high-speed operation and mitigates the copper losses in the end-turns. However, employing a high number of poles introduces challenges related to stator iron losses. The iron loss density is approximately proportional to the square of the electrical frequency and, subsequently, the number of poles, for a given operating magnetic flux density. Although the reduction in stator iron volume with increasing pole number partially offsets this increase in iron losses, the rapid growth of iron losses remains a significant concern. Considering these trade-offs, it is typically advantageous to select pole numbers ranging from four to eight for interior PM machines to strike a balance between various factors and optimize performance. In table 6.1, I have attempted to provide the most important geometric, electromechanical, and thermal characteristics of each machine for the purpose of making comparisons. In the thermal field, I have included only the average temperatures of a slot, because the conductors represent the hottest elements within the machines. To assess the machines' ability to operate at speeds higher than the base speed, specifically in terms of flux weakening capabilities, I chose to present the torque, power losses, and efficiency at a speed of 16000 rpm. Also, I displayed the torque, power factor, power, and efficiency for all the machines at their nominal torque in Figure 6.1.

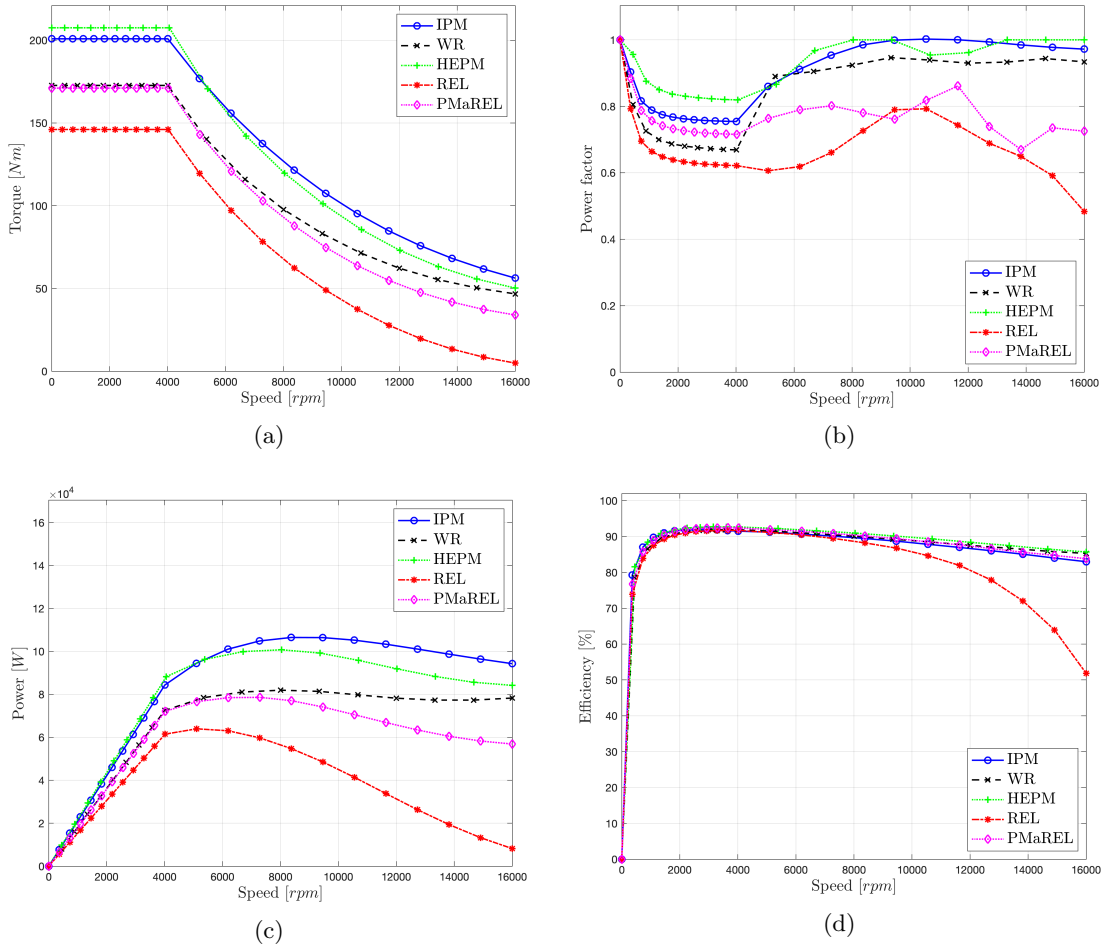

Figure 6.1: Torque, power factor, power and efficiency for IPM, WR, HEPM, REL and PMAREL configurations: (a) torque, (b) power factor, (c) power, (d) efficiency

Table 6.1: Comparison of the 5 motors considering the same DC stator losses

Parameter	**IPM**	**WR**	**HEPM**	**REL**	**PMaREL**
Q_s	72	54	54	54	54
$2p$	12	6	6	6	6
De	242 mm	242 mm	242 mm	242 mm	242 mm
Di	180 mm	160 mm	160 mm	160 mm	160 mm
L_{stk}	132 mm	132 mm	132 mm	132 mm	132 mm
S_{slot}	65.7 mm^2	101.65 mm^2	101.65 mm^2	101.65 mm^2	101.65 mm^2
G_{Cu}	6.35 kg	8.61 kg	8.61 kg	8.61 kg	8.61 kg
G_{fe}	28.1 kg	34.52 kg	33.48 kg	33.76 kg	33.76 kg
PM_{volume}	0.295e-3 m^3	-	0.134e-3 m^3	-	0.8025e-3 m^3
V_{DC}	420 V	410 V	405 V	375 V	380 V
J_s	9.7 A/mm^2	8.33 A/mm^2	8.33 A/mm^2	8.33 A/mm^2	8.33 A/mm^2
J_r	-	6.25 A/mm^2	6.25 A/mm^2	-	-
PJs_{DC}	1682 W	1682 W	1682 W	1682 W	1682 W
$\hat{P_m}$	106.5 kW	81.93 kW	100.7 kW	63.9 kW	78.6 kW
$\hat{\eta}$	93.79 %	93.66 %	93.64 %	92.08 %	93.37 %
L_{d}	0.1168 mH	0.785 mH	0.651 mH	0.902 mH	0.197 mH
L_{q}	0.3636 mH	0.759 mH	0.306 mH	0.2438 mH	0.669 mH
ξ	3.11	1.035	2.13	3.84	3.4
n_B	4000 rpm	4000 rpm	4000 rpm	4000 rpm	4000 rpm
f_B	400 Hz	200 Hz	200 Hz	200 Hz	200 Hz
T_m^B	200.85 Nm	172.7 Nm	207.5 Nm	146.1 Nm	171.1 Nm
P_{in}^B	92.14 kW	78.91 kW	95.25 kW	67.05 kW	78.06 kW
$cos(\phi)^B$	0.75	0.67	0.82	0.62	0.71
PJs_{AC}^B	1815.2 W	1721.8 W	1721.8 W	1721.8 W	1721.8 W
Pfe^B	704.28 W	534.68 W	549.23 W	449.97 W	449.63 W
η_B	91.49 %	91.89 %	92.63 %	91.68 %	93.38 %
T_{ripple}^B	26.43 %	30.2 %	16.44 %	12.69 %	8.4 %
ΔT_{Cu}^B	104 K	110 K	111 K	111.6 K	111.5 K
ΔT_{PM}^B	97 K	-	112 K	-	109 K
f_{16000}	1600 Hz	800 Hz	800 Hz	800 Hz	800 Hz
T_m^{16000}	56.26 Nm	46.71 Nm	50.24 Nm	4.9 Nm	33.94 Nm
PJs_{AC}^{16000}	3781.5 W	2317.9 W	2317.9 W	2317.9 W	2317.9 W
Pfe_{16000}	7845.2 W	4855.5 W	4987.7 W	4086.2 W	4083.1 W
η_{16000}	82.97 %	85.28 %	85.68 %	51.84 %	83.79 %

Several observations can be made from Figure 6.1 and Table 6.1:

- As expected, the IPM motor, having a higher pole number, exhibits a high torque density. However, this characteristic is followed by higher stator iron losses, which in turn impact the temperatures of the winding conductors. The iron losses at 16000 rpm are 1.6 times higher than the WR motor. It is important to remember that WR and HEPM motors have one additional degree of freedom compared to the others, which is the ability to control the rotor excitation current to optimize the operating points at reduced load. In this table, I have only shown the operating conditions at nominal stator current and maximum rotor current. If we were to analyze operating points at reduced torque, especially at speeds higher than the base one, we could appreciate the greater reduction in iron losses by these two motors, making them more appealing than the others.

- In the base point, the HEPM motor is the one that generates the highest torque, approximately 3.31% more than the IPM. However, it is interesting to note that it consumes about 3.37% more electrical power input. Therefore, we can say that its torque density is absolutely comparable to that of the IPM motor, which is an encouraging result for this unusual type of motor. Additionally, the average slot over-temperature is similar, but the power factor and torque ripple of the HEPM are higher than those of the IPM.

- The same argument of the previous point can be made for the WR motor, as the generated torque, although lower than the IPM motor, is proportional to the absorbed electrical power, and the efficiency is similar. If we were to make the WR motor operate at the same torque as the IPM motor, it would certainly heat up more. This is caused by the heat generation from the rotor windings and their distance from the outer shell of the machine.

- A well-known characteristic of reluctance machines is their very low power factor which impacts converter sizing and cost. In this case, the power factor at the base point is approximately 0.6, which turns out to be much lower compared to the other machines. The addition of bonded magnets in this motor (PMaREL) has led to a significant improvement in all its performances; for example, the torque has increased by 17% and the power factor has increased across the entire speed range.

From a control perspective, understanding the magnetic parameters is crucial for designing and controlling synchronous machine drives. Synchronous Reluctance (REL) and PM-assisted Synchronous Reluctance (PMaREL) machines, among others, exhibit highly nonlinear relationships between current and flux linkage due to magnetic saturation. This non linearity includes cross interference between the d and q rotor axes. Analyzing and manipulating the flux maps is valuable throughout the machine's life-cycle, from design to the implementation of control algorithms.

An alternative approach for control is the more popular inductance-based modeling approach. This approach is generally applicable and recommended for machines with significant linearity. Regardless, all synchronous machines have a nonlinear magnetic model, with saturation in the d and q inductances influenced by self-axis current and cross-axis current known as cross-saturation. Precise knowledge of the magnetic model empowers machine and drive designers to optimize torque density, efficiency, flux weakening capability, dynamic response, and potential for self-sensing control [14].

Following that, an analysis of the flux maps of the five examined motors is conducted to identify which motors can be regarded as relatively linear and which cannot.

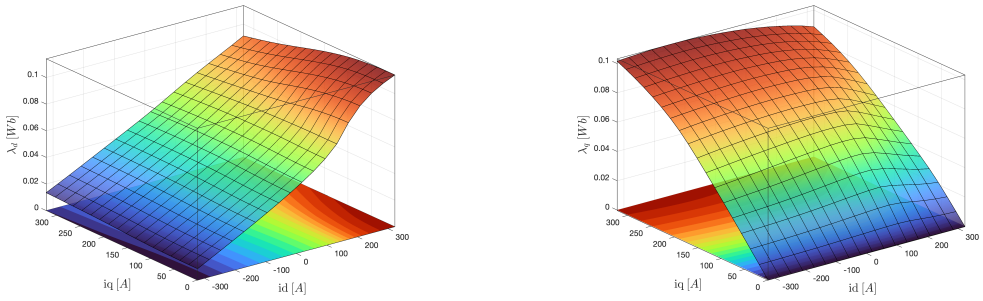

(a) (b)

Figure 6.2: Flux linkage maps of IPM: (a) d-axis flux linkage, (b) q-axis flux linkage

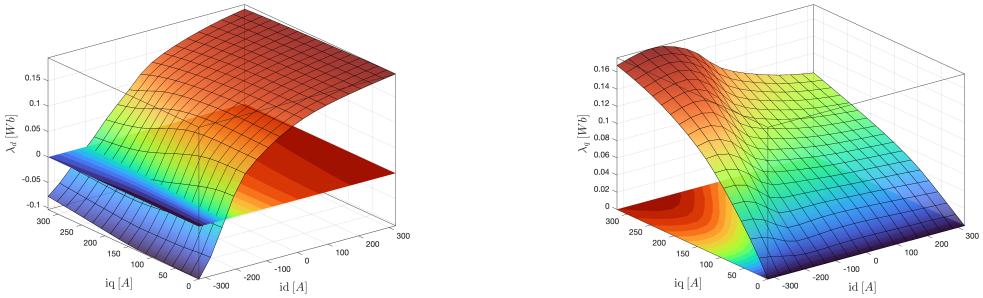

(a) (b)

Figure 6.3: Flux linkage maps of WR: (a) d-axis flux linkage, (b) q-axis flux linkage

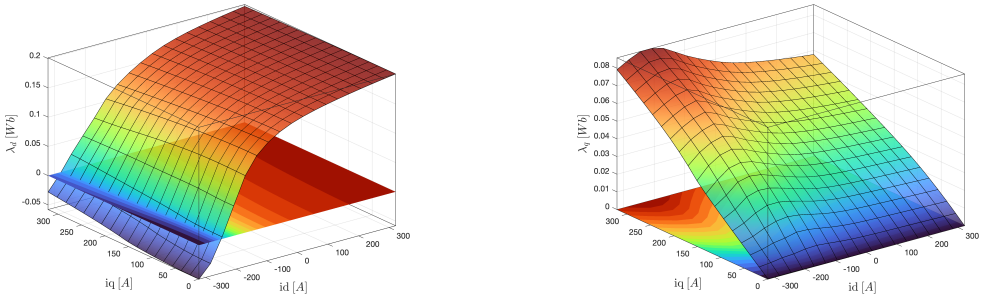

(a) (b)

Figure 6.4: Flux linkage maps of HEPM: (a) d-axis flux linkage, (b) q-axis flux linkage

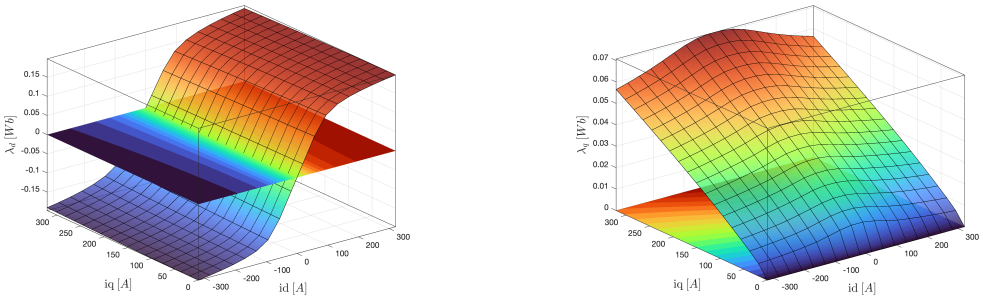

(a) (b)

Figure 6.5: Flux linkage maps of REL: (a) d-axis flux linkage, (b) q-axis flux linkage

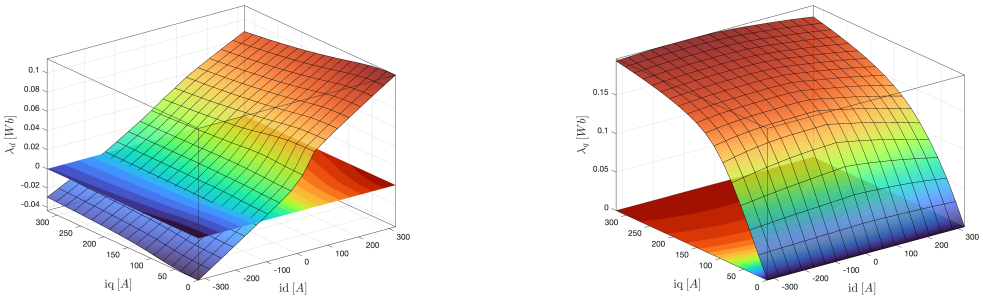

(a) (b)

Figure 6.6: Flux linkage maps of PMaREL: (a) d-axis flux linkage, (b) q-axis flux linkage

All the analyzed machines exhibit noticeable curvatures, indicating non-constant parameters. Among them, the REL motor demonstrates the most prominent non-linearity, especially on the d-axis. The utilization of the inductance model proves to be impractical for the design and control of the PM/REL machine.

Chapter 7

Conclusions

When it comes to applications requiring the highest efficiency, compact size, minimal complexity, and reduced weight, well-designed permanent magnet synchronous machines with high-strength rare-earth magnets are extremely difficult to surpass compared to other types of machines. However, if the application allows for trade-offs in performance requirements in favor of lower cost or other factors, alternative machine types can become highly competitive.

Each of the topologies presented here has its own advantages and disadvantages, emphasizing the importance of specific application requirements in making the appropriate choice. Synchronous reluctance machines, which eliminate the need for magnets entirely, offer appealing lower cost and rotor robustness. However, they present significant design challenges due to the requirement for maximum magnetic saliency to enhance power factor, efficiency, and torque/power density. As a result, they struggle to compete with well-designed induction machines or permanent magnet synchronous machines in traction electric applications, as no well-known manufacturer has employed them in this field.

In situations where low cost, simple control, and efficiency take precedence over torque and power density, the PMaREL (Permanent Magnet and Reluctance) machine could be a viable option. On the other hand, for high controllability across a wide operating range, the Wound Rotor machine is an alternative worth considering. However, challenges such as rotor winding cooling and minimizing additional volume and maintenance requirements for supplying rotor current need to be addressed.

While some of the topologies discussed in this study are mature and widely used, others are still in the early stages of development. Each of them shows promise in its own way but requires further research and development to reach its full potential.

Appendix A

Efficiency map computation

The efficiency map is a highly effective graphical representation used to describe the performance of an electric machine. It presents a constant-efficiency contour plot in the torque or power versus speed plane. Each point on the map corresponds to a specific current supply condition that achieves the maximum efficiency for a given torque and speed load point.

Mathematically, the efficiency map can be represented as a 2D matrix with rows (R) and columns (C). The indices i and j represent the row and column indices, respectively. The number of rows and columns in the matrix depends on the chosen size of the torque and speed arrays used to construct the evenly spaced grid.

The maximum torque value considered in the efficiency map is determined by the operating condition and current limit of the machine. It can be set to the rated torque or the overload torque, depending on the specific situation. Similarly, the maximum speed is determined by the mechanical constraints of the machine.

It is important to note that the efficiency map computation automatically takes into account the voltage. The efficiency values calculated in the map consider the voltage as a factor influencing the machine's performance at different operating points.

The two arrays are defined as follows:

$$T_m = \begin{pmatrix} Tm^{(1)} \\ Tm^{(2)} \\ \vdots \\ Tm^{(R)} \end{pmatrix}, \qquad \omega_m = (\omega_m^{(1)}, \omega_m^{(2)}, \ldots, \omega_m^{(C)}) \tag{A.1}$$

which means that the (i,j) element of the efficiency map, η, contains the maximum efficiency achievable with the torque, $Tm^{(i)}$, at the mechanical speed, $\omega_m^{(j)}$.

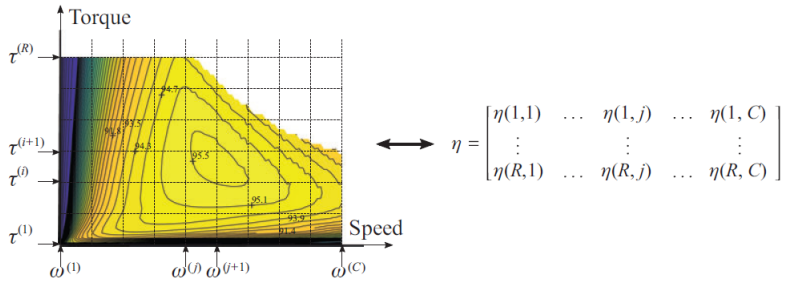

Figure A.1: Efficiency map in the torque versus speed plane example [5]

In the case of synchronous machines, there are numerous combinations of Id and Iq currents that can generate the torque $Tm^{(i)}$ at the speed $\omega_m^{(j)}$, while still operating within the limits of current and voltage. However, determining the optimal Id and Iq combination that results in the maximum efficiency is the main challenge in computing the efficiency map.

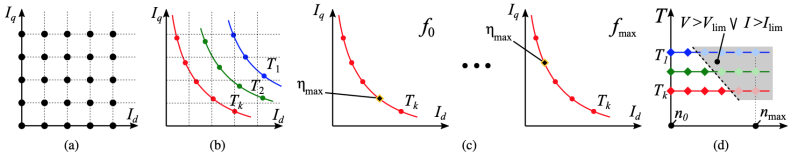

Figure A.2: Steps for the computation of the efficiency map: (a) Sampled points in the (id,iq) plane, (b) Constant-torque loci in the (id,iq) plane, (c) Maximum efficiency on constant-Tk locus at different frequencies and (d) Constant-torque liens in the (T,n) plane. [1]

Appendix B

Iron losses computation

The most commonly used mathematical formulation for iron losses is an extension of the classical Steinmetz equation. This equation includes two terms: one that varies linearly with frequency and another that depends on the frequency squared. These terms represent hysteresis losses and eddy current losses, respectively:

$$p_{FE} = c_{hy}(\frac{f}{f^*})(\frac{B}{B^*})^2 + c_{ec}(\frac{f}{f^*})^2(\frac{B}{B^*})^2 \tag{B.1}$$

Here, c_{hy} and c_{ec} are the coefficients for hysteresis and eddy current losses, respectively. Since both terms depend on B^2, we need to vary the frequency to determine these coefficients. There are several methods to obtain c_{hy} and c_{ec}, with the two most common approaches being interpolation and the least squares method. In this description, we will focus on the interpolation method.

To apply the interpolation method, we select two pairs of flux density and frequency values, denoted as $(B_i, f_i)_{i=1,2}$, along with their corresponding power loss density p_i. To give an example, let's take into account the sheet metal employed for the machines analyzed in this study.

Table B.1: Specific iron losses for M-19 29 Gauge Steel

Conditions	Specific losses	Unit
Frequency 50 [Hz]		
Flux density 1.2 [T]	1.515	[W/kg]
Frequency 1000 [Hz]		
Flux density 1.2 [T]	119.6	[W/kg]

Considering:

$$\begin{aligned} B^* &= 1.2[T] \\ f^* &= 50[Hz] \end{aligned} \tag{B.2}$$

We can set up the following system of equations:

$$\begin{cases} 1.515 &= c_{hy}(\frac{50}{f^*})(\frac{1.2}{B^*})^2 + c_{ec}(\frac{50}{f^*})^2(\frac{1.2}{B^*})^2 \\ 119.6 &= c_{hy}(\frac{1000}{f^*})(\frac{1.2}{B^*})^2 + c_{ec}(\frac{1000}{f^*})^2(\frac{1.2}{B^*})^2 \end{cases} \tag{B.3}$$

Since all the terms in the system are known except for c_{hy} and c_{ec}, we can solve it directly to obtain the coefficients:

$$c_{hy} = 1.28[W/kg]$$
$$c_{ec} = 0.235[W/kg] \tag{B.4}$$

It is chosen to vary the frequency from 50 [Hz] to 2000 [Hz] and the flux density from 0 [T] to 2 [T]. The resulting iron losses are represented in Fig. B.1. We can observe that specific losses increases as frequency or flux density increases.

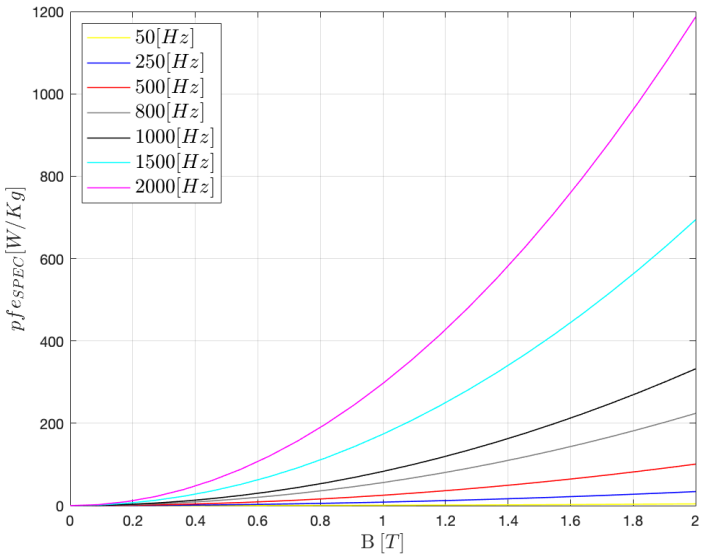

Figure B.1: Iron losses varying frequency and flux density

Appendix C

Hairpin windings: losses computation

Two common methods for calculating these losses are analytical and numerical approaches.

C.1 Analytical analysis

A fast way to compute AC copper losses is to use an analytical formulation considering a single slot with n_w conductors as in Fig. C.1

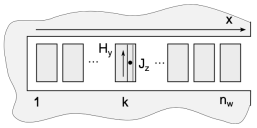

Figure C.1: Reference frame to analytically compute the current density distribution within the rectangular slot

We start by defining the skin depth:

$$\delta = \frac{1}{\sqrt{\pi f \sigma \mu}} \tag{C.1}$$

According to the conductor's height, is useful to introduce the following ratio, called reduced height:

$$\xi = \sqrt{n_w \frac{w_p}{w_s}} \frac{h_p}{\delta} \tag{C.2}$$

This ratio can be adopted to determine the resistance increase and the AC losses through the following functions:

$$\begin{cases} \phi(\xi) = \xi \frac{sinh(2\xi)+sin(2\xi)}{cosh(2\xi)+cos(2\xi)} \\ \psi(\xi) = 2\xi \frac{sinh(\xi)-sin(\xi)}{cosh(\xi)+cos(\xi)} \end{cases} \tag{C.3}$$

Finally, the AC resistance increase of each layer n results:

$$k_{AC,n} = \phi + (k^2 - k)\psi \tag{C.4}$$

this factor is a-dimensional and it represents and additional terms to be multiplied for the DC

resistance in order to compute the overall resistance.

$$k_{AC} = \frac{mean(k_{AC,n}) * L_{stk} + L_{ew}}{L_{stk} + L_{ew}} \tag{C.5}$$

$$R_{AC} = k_{AC} * R_{DC} \tag{C.6}$$

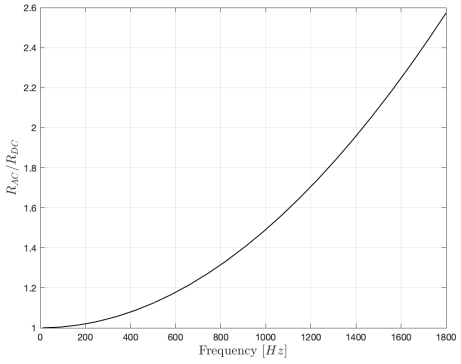

Figure C.2: Analytically computed AC resistance increase @ T=120°C.

C.2 Numerical analysis

The current density distribution of an hairpin winding is reported in Figure C.3, the FEM simulation was conducted by supplying the same current to 8 conductors at a frequency of 500 Hz. It is possible to appreciate a greater accumulation of current near the slot opening.

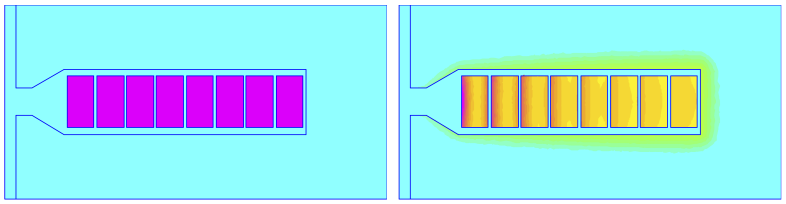

Figure C.3: Current density at 1 Hz and 500 Hz respectively

Fig. C.4 displays the distribution of current density in the y-direction, relative to the slot height. As a result of the proximity effect, the current density distribution is not uniform within each conductor and is concentrated on the sides of the conductors. Furthermore, non-uniform current density is particularly significant in conductors located close to the open slot area, due to the high leakage flux density.

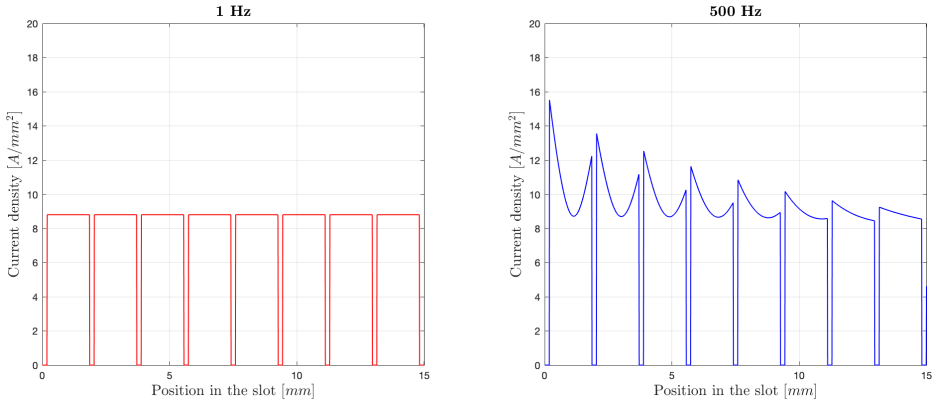

Figure C.4: Current density plot in the y-direction at 1 Hz and 500 Hz respectively

Table C.1: Conductors ohmic losses $[W]$ at 1 Hz and 500 Hz (120 ℃)

freq.	8	7	6	5	4	3	2	1	Slot	$k_{AC/DC}$
1Hz	0.6883	0.6883	0.6883	0.6883	0.6883	0.6883	0.6883	0.6883	5.5061	1
500Hz	1.0054	0.9141	0.8461	0.7913	0.7487	0.7178	0.6981	0.6894	6.4107	1.1643

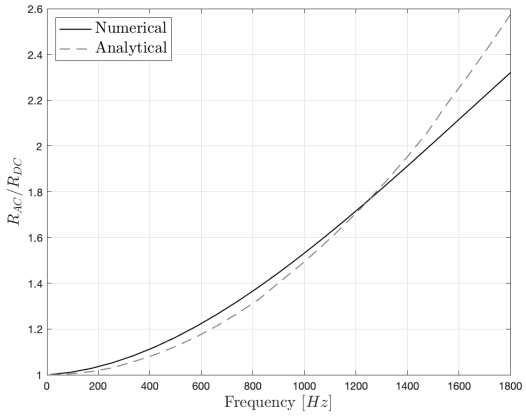

Figure C.5: AC resistance increase comparison @ T=120°C.

Bibliography

[1] Bacco, G., Babetto, C., Bonfante, M., Carbonieri, M., and Bianchi, N. (2019). Efficiency maps computation and comparison including thermal limits. In *2019 IEEE Energy Conversion Congress and Exposition (ECCE)*, pages 4846–4852. IEEE.

[2] Banner, J. (2023). No Magnets, Big Power: BMW's Fifth-Generation Electric Motor. `https://www.motortrend.com/news/bmw-ix-m60-brushed-electric-motor-tech-deep-dive`.

[3] Berardi, G., Nategh, S., Bianchi, N., and Thioliere, Y. (2020). A comparison between random and hairpin winding in e-mobility applications. In *IECON 2020 The 46th Annual Conference of the IEEE Industrial Electronics Society*, pages 815–820. IEEE.

[4] Bianchi, N. (2001). *Calcolo delle macchine elettriche col metodo degli elementi finiti*. Cleup.

[5] Bianchi, N., Babetto, C., and Bacco, G. (2021). *Synchronous Reluctance Machines: Analysis, Optimization and Applications*, volume 186. IET.

[6] Bianchi, N., Carlet, P. G., Cinti, L., and Ortombina, L. (2022). A review about flux-weakening operating limits and control techniques for synchronous motor drives. *Energies*, 15(5):1930.

[7] Gierczynski, M. and Grzesiak, L. (2019). Per unit approach based assessment of torque production capability of pmsms operating in the field weakening region. In *2019 Fourteenth International Conference on Ecological Vehicles and Renewable Energies (EVER)*, pages 1–15. IEEE.

[8] Guemo, G. G., Chantrenne, P., and Jac, J. (2013). Application of classic and t lumped parameter thermal models for permanent magnet synchronous machines. In *2013 International Electric Machines & Drives Conference*, pages 809–815. IEEE.

[9] Hendershot, J. (2017). Connect tutorial E-Car Project Insight: BMW i3 Electric Traction Drive. [YouTube video]. `http://www.youtube.com/watch?v=xt-nfcwv6Kc`.

[10] Hwang, D. and Gu, B.-G. (2020). Field current control strategy for wound-rotor synchronous motors considering coupled stator flux linkage. *IEEE Access*, 8:111811–111821.

[11] Martens, M. and König-Petermaier, K. (2020). Influence of rotor current on noise excitation in electrically-excited synchronous machines. In *2020 IEEE Vehicle Power and Propulsion Conference (VPPC)*, pages 1–5. IEEE.

[12] Oak Ridge National Laboratory (2017). FY 2016 Annual Progress Report for Electric Drive Technologies Program. [Online].

[13] Panda, S., Keshri, R. K., Tessarolo, A., Tiwari, G., and Mezzarobba, M. (2020). Design refinements of synchronous reluctance motor utilising non-magnetic radial ribs for traction applications. *IET Electric Power Applications*, 14(12):2480–2489.

[14] Pellegrino, G., Jahns, T. M., Bianchi, N., Soong, W. L., and Cupertino, F. (2016). The rediscovery of synchronous reluctance and ferrite permanent magnet motors: tutorial course notes.

[15] Rossi, C., Casadei, D., Pilati, A., and Marano, M. (2006). Wound rotor salient pole synchronous machine drive for electric traction. In *Conference Record of the 2006 IEEE Industry Applications Conference Forty-First IAS Annual Meeting*, volume 3, pages 1235–1241. IEEE.